

SANDIA REPORT

SAND2008-6089

Unlimited Release

September 2008

Simulating the Pervasive Fracture and Fragmentation of Materials and Structures using Randomly Close-Packed Voronoi Tessellations

Joseph E. Bishop

Prepared by
Sandia National Laboratories
Albuquerque, New Mexico 87185 and Livermore, California 94550

Sandia is a multiprogram laboratory operated by Sandia Corporation, a Lockheed Martin Company, for the United States Department of Energy's National Nuclear Security Administration under Contract DE-AC04-94AL85000.

Approved for public release; further dissemination unlimited.



Issued by Sandia National Laboratories, operated for the United States Department of Energy by Sandia Corporation.

NOTICE: This report was prepared as an account of work sponsored by an agency of the United States Government. Neither the United States Government, nor any agency thereof, nor any of their employees, nor any of their contractors, subcontractors, or their employees, make any warranty, express or implied, or assume any legal liability or responsibility for the accuracy, completeness, or usefulness of any information, apparatus, product, or process disclosed, or represent that its use would not infringe privately owned rights. Reference herein to any specific commercial product, process, or service by trade name, trademark, manufacturer, or otherwise, does not necessarily constitute or imply its endorsement, recommendation, or favoring by the United States Government, any agency thereof, or any of their contractors or subcontractors. The views and opinions expressed herein do not necessarily state or reflect those of the United States Government, any agency thereof, or any of their contractors.

Printed in the United States of America. This report has been reproduced directly from the best available copy.

Available to DOE and DOE contractors from

U.S. Department of Energy
Office of Scientific and Technical Information
P.O. Box 62
Oak Ridge, TN 37831

Telephone: (865) 576-8401
Facsimile: (865) 576-5728
E-Mail: reports@adonis.osti.gov
Online ordering: <http://www.osti.gov/bridge>

Available to the public from

U.S. Department of Commerce
National Technical Information Service
5285 Port Royal Rd.
Springfield, VA 22161

Telephone: (800) 553-6847
Facsimile: (703) 605-6900
E-Mail: orders@ntis.fedworld.gov
Online order: <http://www.ntis.gov/help/ordermethods.asp?loc=7-4-0#online>



Simulating the Pervasive Fracture and Fragmentation of Materials and Structures using Randomly Close-Packed Voronoi Tessellations

Joseph E. Bishop
Strategic Initiatives
Sandia National Laboratories
P.O. Box 5800
Albuquerque, New Mexico 87185-MS0346

Abstract

Under extreme loading conditions most often the extent of material and structural fracture is pervasive in the sense that a multitude of cracks are nucleating, propagating in arbitrary directions, coalescing, and branching. Pervasive fracture is a highly nonlinear process involving complex material constitutive behavior, material softening, localization, surface generation, and ubiquitous contact. Two primary applications in which pervasive fracture is encountered are (1) weapons effects on structures and (2) geomechanics of highly jointed and faulted reservoirs.

A pure Lagrangian computational method based on randomly close-packed Voronoi tessellations is proposed as a rational approach for simulating the pervasive fracture of materials and structures. Each Voronoi cell is formulated as a finite element using the reproducing kernel method. Fracture surfaces are allowed to nucleate only at the intercell faces. The randomly seeded Voronoi cells provide an unbiased network for representing cracks. In this initial study two approaches for allowing the new surfaces to initiate are studied: (1) dynamic mesh connectivity and the instantaneous insertion of a cohesive traction when localization is detected, and (2) a discontinuous Galerkin approach in which the interelement tractions are an integral part of the variational formulation, but only become active once localization is detected.

Pervasive fracture problems are extremely sensitive to initial conditions and system parameters. Dynamic problems exhibit a form of transient chaos. The primary numerical challenge for this class of problems is the demonstration of model objectivity and, in particular, the identification and demonstration of a measure of convergence for engineering quantities of interest.

ACKNOWLEDGMENTS

The many discussions with Professor Mark Rashid at UC Davis on finite element formulations of polyhedral elements are gratefully acknowledged. The discussions with both Professor Gianluca Cusatis at Rensselaer Polytechnic Institute and Dr. James Cox at Sandia on concrete modeling and validation testing are gratefully acknowledged. The discussions with Professor Rebecca Brannon at University of Utah on the ramifications of material softening to objectivity and mesh independence are gratefully acknowledged.

CONTENTS

LIST OF FIGURES	5
1. INTRODUCTION	9
2. RANDOMLY CLOSE-PACKED VORONOI TESSELLATIONS	13
3. POLYHEDRAL ELEMENT FORMULATION	17
4. DYNAMIC MESH CONNECTIVITY AND CONTACT	25
5. LIMITS OF PREDICTABILITY AND CONVERGENCE	27
6. EXAMPLE	31
7. DISCRETE FRACTURE ABSTRACTIONS	43
7.1 FRACTURE STATE SPACE.....	43
7.2 GRAPH THEORY AND PERCOLATION.....	46
8. VALIDATION APPROACH	49
9. DISCONTINUOUS-GALERKIN FORMULATION	53
9.1 LAGRANGE MULTIPLIER BASED DISCONTINUOUS GALERKIN	53
9.2 NITSCHKE BASED DISCONTINUOUS GALERKIN.....	54
10. SUMMARY	57
11. REFERENCES	59

LIST OF FIGURES

Figure 1. A collection of points and their associated Voronoi diagram defined by Eq.(1).....	14
Figure 2. The associated Voronoi diagram for both an hexagonal close packed array of points (a) and a randomly close packed array (b). The resulting cell structures tessellate the domain using 126 cells.	14
Figure 3. Process used to create the randomly close packed Voronoi tessellation: (a) random seeding until the theoretical maximum packing is reached with a constraint on minimum distance between points, (b) Delaunay triangulation, and (c) dual Voronoi tessellation.	15
Figure 4. Regularization of the Voronoi tessellation by removing relatively small edges and equivalencing nodes: (a) raw Voronoi tessellation and (b) Voronoi mesh with constraint on minimum edge size. The histogram of the number of elements for a given number of edges is also given.....	16
Figure 5. (a) Contour plot of the nodal weight function for an interior node of a regular hexagonal mesh. The weight function is obtained by solving the local boundary value problem defined by Eq. (11). (b) Contour plot of the shape function resulting from the application of the reproducing kernel methodology.	19
Figure 6. Effect of discrete integration consistency on the L_2 norm of the displacement error for the beam-bending verification problem using a regular hexagonal mesh with cell size h (plane stress, Poisson's ratio = 0.3, beam aspect ratio = 4.62).	21
Figure 7. Sensitivity of the L_2 norm of the displacement error to perturbations in the regular hexagonal mesh for the beam-bending verification problem (plane stress, Poisson's ratio = 0.3).....	22
Figure 8. Effect of Poisson's ratio on the L_2 norm of the displacement error for the beam-bending verification problem using a mean dilation formulation and a distorted hexagonal mesh ($r = 0.2$, plane strain).	23

Figure 9. Effect of number of element integration points on the L_2 norm of the displacement error for the beam-bending verification problem using a distorted hexagonal mesh ($r = 0.2$, plane stress).....	24
Figure 10. A low strength concrete column striking a rigid wall at a 45 degree angle.....	32
Figure 11. Mohr-Coulomb failure surface in shear (τ) normal-stress (σ) space, with cohesion c , tensile cutoff σ_o , and internal friction μ	32
Figure 12. Randomly close packed Voronoi realizations for three different characteristic cell sizes, $h = 8.0$, $h = 4.0$, and $h = 2.0$. Three realizations are shown for each characteristic cell size.....	33
Figure 13. Deformed state and crack surfaces of the concrete column at a number of instances in time after impact with an impact angle of 45.00° ($R_1^{2.0}$ mesh). Only cracks that have fully softened (no cohesive tractions) are shown. Impact times are 2, 10, 30, 150, and 230 ms.....	34
Figure 14. Deformed state and crack surfaces of the concrete column at a number of instances in time after impact with an impact angle of 49.99° ($R_1^{2.0}$ mesh). Only cracks that have fully softened (no cohesive tractions) are shown. Impact times are 2, 10, 30, 150, and 230 ms.....	35
Figure 15. Cumulative distribution of the fragment mass-fraction at a simulation time of 300 ms for the $R_i^{2.0}$, $i \in \{1,2,3, \dots, 12\}$ RCP Voronoi mesh family with homogeneous material properties. The mean of the <i>maximum</i> -fragment mass-fraction is denoted by the arrow.....	37
Figure 16. Cumulative distribution of the fragment mass-fraction at a simulation time of 300 ms using the $R_1^{2.0}$ mesh with twelve material realizations of a $\pm 5\%$ uniform variation on elastic modulus and Mohr-Coulomb failure surface. The homogenous material case is given for comparison.....	38
Figure 17. Cumulative distribution of the fragment mass-fraction at a simulation time of 300 ms for the $R_i^{8.0}$, $i \in \{1,2,3, \dots, 12\}$ RCP Voronoi mesh family with homogeneous material properties. The mean of the <i>maximum</i> -fragment mass-fraction is denoted by the arrow.....	39
Figure 18. Cumulative distribution of the fragment mass-fraction at a simulation time of 300 ms for the $R_i^{4.0}$, $i \in \{1,2,3, \dots, 12\}$ RCP Voronoi mesh family with homogeneous material properties. The mean of the <i>maximum</i> -fragment mass-fraction is denoted by the arrow.....	40
Figure 19. Cumulative distribution of the fragment mass-fraction at a simulation time of 300 ms for the $R_i^{1.0}$, $i \in \{1,2,3, \dots, 12\}$ RCP Voronoi mesh family with homogeneous material properties. The mean of the <i>maximum</i> -fragment mass-fraction is denoted by the arrow.....	41
Figure 20. The <i>maximum</i> fragment size for twelve RCP Voronoi mesh realizations at four mesh resolutions $R_i^{8.0}$, $R_i^{4.0}$, $R_1^{2.0}$, and $R_i^{1.0}$ with homogeneous material properties. For each mesh resolution the mean of the maximum fragment mass-fraction is also given.....	42
Figure 21. Crack states resulting from a rigid projectile impacting a concrete column. Each image represents the results from a different simulation using the same RCP Voronoi mesh but with a slightly different striking velocity. The time is 3.0 ms after impact which corresponds to the final simulation step (6400) reported in Figure 22.....	45
Figure 22. Distance between crack states resulting from a rigid projectile impacting a concrete column (see Figure 21) as a function of simulation step. Each curve represents a different simulation using the same RCP Voronoi mesh but with a slightly different striking velocity. Distances are with respect to the reference simulation shown at the top of Figure 21 (striking velocity = 20.0 m/s). The final simulation step (6400) corresponds to the time of 3.0 ms used in Figure 21.....	46
Figure 23. Schematic of a displacement controlled three-point bend test.....	49

Figure 24. Simulation of a displacement controlled three-point bend experiment (a) RCP Voronoi mesh graded near the center with contoured max-principal stress field (b-d) Three separate simulations of crack growth using three different RCP Voronoi meshes with identical loading conditions.50

Figure 25. Schematic illustrating the interelement tractions obtained from the adjacent mean element stress.55

Figure 26. Comparison of the L_2 norm of the displacement error for the beam-bending verification problem using both a standard continuous Galerkin formulation and a discontinuous Galerkin formulation. Ten RCP Voronoi mesh realizations were used at each refinement level where h_{average} represents the average cell size of the RCP Voronoi mesh. Results for the discontinuous Galerkin formulation are given for several values of the penalty parameter k_p . The convergence rate is also given. (plane stress conditions, Poisson's ratio = 0.3, beam aspect ratio = 4.0).....56

1. INTRODUCTION

Possible structural responses from extreme loading conditions, such as blast loads, can range from intact vibrational response to complete fragmentation. A structure transitions from an intact continuum to a discontinuum through crack initiation and propagation. The extent of fracturing is termed pervasive when a multitude of cracks arbitrarily nucleate, propagate, coalesce, and branch. The simulation of pervasive structural failure is further complicated by the ubiquitous self contact that accompanies new crack surfaces. In order to design structures to withstand extreme loading conditions it is imperative to have accurate computational solid mechanics methodologies for simulating pervasive failure. Any computational methodology that strives to model pervasive failure must include the ability to numerically represent the progression of a body from a continuum description to a discontinuum description. In addition any computational methodology must be objective such that the simulation results do not depend on subjective properties of the model such as mesh design. One necessary condition for simulation objectivity is that the numerical approximation converges with discretization refinement. Without convergence to the necessary ‘engineering accuracy,’ numerical results and predictions are suspect, rendering validation, uncertainty quantification efforts, and general use in engineering design suspect as well.

Currently, there is a very limited set of computational tools available that can attempt to simulate the pervasive failure of structures. Common and often unsatisfactory techniques include ‘element death’ in Lagrangian finite element codes and ‘void insertion’ in hydrocodes. The enriched finite element methods (generalized finite element method and extended finite element method) have had success in modeling dilute fracture problems [1,2]. Once crack branching and crack coalescence phenomena appear, the prospect of modeling a multitude of arbitrary three-dimensional intersecting cracks quickly becomes untenable. A variety of meshless or particle methods have been developed in the past fifteen years with the goal of modeling extreme deformation of solids including pervasive failure [3]. Examples include spherical particle hydrodynamics [4], element free Galerkin [5], reproducing kernel method [6], cracked particles [7], material point method [8], peridynamics [9], particle in element [10], and element to particle conversion [11]. In general, these methods have had success in modeling certain classes of pervasive failure, e.g. perforation. In contrast, Ortiz and coworkers [12–17] have pursued the concept of using standard finite element methods for modeling pervasive failure, in particular, tetrahedral meshes, but with fracture surfaces allowed to nucleate and propagate only along the interelement faces. At the inception of material softening and localization the mesh connectivity is modified to reflect the new surface and a cohesive traction with a softening behavior is dynamically inserted. This seemingly severe restriction of only allowing fracture surfaces to nucleate at interelement faces, as opposed to unrestricted methods modeling single crack growth, offers several advantages in the simulation of pervasive failure. In a continuum the intersection of multiple arbitrarily intersecting *general* crack surfaces can result in subdomains whose surface topology is ill-posed for further computation. The restriction of only allowing new surfaces to form at interelement faces provides a necessary regularization of the resulting domain and surface topologies. For example, variational methods for solving the governing equations of motion, e.g. the finite element method, require that the domain have a Lipschitz continuous boundary. Thus, as the original domain fractures and disassociates into subdomains, each subdomain needs to have a Lipschitz continuous boundary as well. Also, the resulting subdomains

could be arbitrarily small making further computation impossible in an explicit-dynamics framework. The restriction of only allowing new surfaces to form at interelement faces provides *a priori* the constraint on minimum edge size and subsequent critical-time step necessary in an explicit dynamic numerical solution. Furthermore, the restriction of only allowing new surfaces to form at interelement faces results in a time varying domain whose volume is continuous in time. This is not the case in most particle methods whose continuum representation evolves into a collection of spheres. (Recall that the theoretical maximum packing for equi-sized spheres is only 74%.) This continuity of volume in time can be very important in confined problems such as penetration and reconsolidation.

In this report a pure Lagrangian computational method is proposed for modeling pervasive fracture. Fracture surfaces are allowed to nucleate and propagate only along interelement faces of a domain mesh. The use of an unstructured mesh, even an unstructured tetrahedral mesh, is potentially biased with respect to edge and face orientation which could lead to nonobjective numerical predictions. Ideally, the face structure should be completely random to remove any bias. Instead of using a tetrahedral mesh, a randomly close packed (RCP) Voronoi tessellation [18] of the domain is used. The resulting random face network provides an unbiased computational basis for representing fracture surfaces in a homogenous isotropic continuum. The polyhedral cells of the RCP Voronoi tessellation are formulated as finite elements using the reproducing kernel method [6]. The resulting polyhedral elements have a number of desirable properties including convexity and relatively large included angles. This latter property is expected to result in increased robustness in large deformation analyses of ductile materials. Additionally, the Voronoi face network provides a convenient discrete structure for studying fracture surface topology and percolation like processes during impact and fragmentation.

Two approaches for allowing the new fracture surfaces to initiate are studied: (1) dynamic connectivity and the instantaneous insertion of a cohesive traction when localization is detected, and (2) a discontinuous Galerkin approach in which all finite elements are disconnected and the interelement tractions are an integral part of the variational formulation but only become active once localization is detected. The former is computationally efficient but exhibits undesirable artificial vibrational behavior in low-energy problems due to fundamental inconsistencies between nodal forces assembled from element stresses and interelement tractions obtained from element stresses. The latter method has the potential to be much smoother in time but is still an active area of research.

The primary objectives of this report are (1) to propose the use of randomly close-packed Voronoi tessellations for simulating pervasive fracture and (2) to elucidate the difficulties in defining and demonstrating convergence for this class of problems. Future work will focus on validation. This paper is organized as follows. The randomly close-packed Voronoi tessellation is described in Section 2. Section 3 discusses the polyhedral finite element formulation based on the reproducing kernel method. Section 4 gives an overview of the dynamic mesh connectivity algorithm and an overview of the self-contact algorithm. A discussion on the limits of predictability for pervasive failure problems along with proposed weaker definitions of convergence from statistical theory is given in Section 5. A two dimensional example of a quasi-brittle structure impacting a rigid surface is presented in Section 6 based on the dynamic mesh connectivity approach. Further abstractions enabled by a discrete fracture representation are

presented in Section 7. Section 8 discusses an initial validation approach choosing concrete as the material of interest. Section 9 presents the discontinuous Galerkin approach for incorporating cohesive tractions. A summary is given in Section 10.

2. RANDOMLY CLOSE-PACKED VORONOI TESSELLATIONS

Voronoi tessellations have a rich history in mathematics and science and have a number of advantageous properties [19]. Given a finite set of points $\{\mathbf{X}_i\}$ or nuclei, the Voronoi tessellation is defined as the collection of regions or cells V_i where

$$V_i = \bigcap_{i \neq j} \{ \mathbf{X} \mid d(\mathbf{X}_i, \mathbf{X}) < d(\mathbf{X}_j, \mathbf{X}) \} \quad (1)$$

Here, \mathbf{X} represents an arbitrary point in the domain, and the function d is the Euclidean distance between two points. Each spatial point belonging to the Voronoi cell i is closer to nucleus i than all other nuclei. Note that each Voronoi cell is defined as the intersection of half-spaces and is thus convex. An example of a two dimensional Voronoi cell is shown in Figure 1. While the Voronoi tessellation can be formed from any finite set of points or seeds, a special structure arises from the study of close packing of equi-sized hard spheres [20]. A classic experiment of dropping hard spheres into a relatively large container produces a structure known as random close-packed (RCP) [18]. Unlike the well known hexagonal close-packed (HCP) structure with a packing factor of 0.740, the RCP structure exhibits a *maximum* packing factor of only 0.637. An example of the associated Voronoi tessellation for both the HCP and RCP structures in two dimensions is shown in Figure 2. The RCP structure arises in a number of scientific fields and has been extensively studied. The RCP structure provides a foundation for the study of amorphous solids as described by Zallen [18]. The statistical geometry aspects of RCP structures and their associated Voronoi diagrams have been studied by Finney [21]. In three dimensions the *average* number of nearest neighbors is 14.3. For comparison, the number of nearest neighbors of the hexagonal close-packed structure is exactly 14. For the RCP structure the *average* aspect ratio of each Voronoi cell is approximately one. The median number of cell faces is 14 with a large majority of the face distribution in the range of 13 to 16. The median number of edges of each cell face is 5 with a large majority of the distribution in the 4 to 6 range. Most importantly each junction or node of the RCP Voronoi structure is randomly oriented with only a short range correlation to neighboring nodes. Thus, with respect to crack propagation along the Voronoi face network, it is expected that the RCP Voronoi structure will provide an unbiased and perhaps optimal face basis for representing semi-arbitrary crack growth in an isotropic medium. In two dimensions the RCP Voronoi structure results in cells with an *average* number of edges of exactly 6 and an average interior vertex angle of approximately 120° [18]. These relatively large interior angles compared to conventional triangle and quadrilateral meshes are expected to result in relatively robust behavior in problems with large strain gradients.

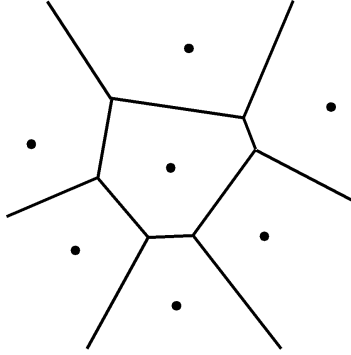


Figure 1. A collection of points and their associated Voronoi diagram defined by Eq.(1).

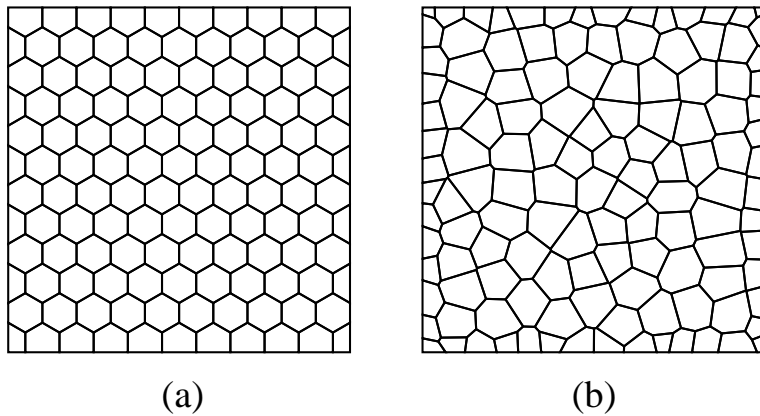


Figure 2. The associated Voronoi diagram for both an hexagonal close packed array of points (a) and a randomly close packed array (b). The resulting cell structures tessellate the domain using 126 cells.

Bolander and coworkers [22–25] have used RCP Voronoi tessellations in spring-lattice models to simulate quasistatic crack growth in an isotropic medium. Their process for generating the RCP Voronoi seeds is followed here with only minor modifications. For a given characteristic length h , points are randomly and sequentially placed in the domain with a constraint on minimum distance between points. The constraint is enforced by merely discarding those new points that violate the constraint. The seeding process stops when the maximum packing threshold is reached within tolerance. Given the RCP point distribution, a number of techniques can be used to generate the Voronoi tessellation. Here, the domain is first triangulated using the Bowyer-Watson insertion algorithm resulting in a Delaunay triangulation (see Figure 3) [26,27]. The Voronoi diagram is simply the dual of the Delaunay triangulation in the sense that the Voronoi cell nuclei are the vertices of the Delaunay triangulation, and the vertices of the Voronoi cells are the circumcenters of the Delaunay triangles. The generation of the Voronoi diagram is straight forward in unbounded domains but is nontrivial near geometrically ‘complex’ boundaries due to the need for intersection operations.

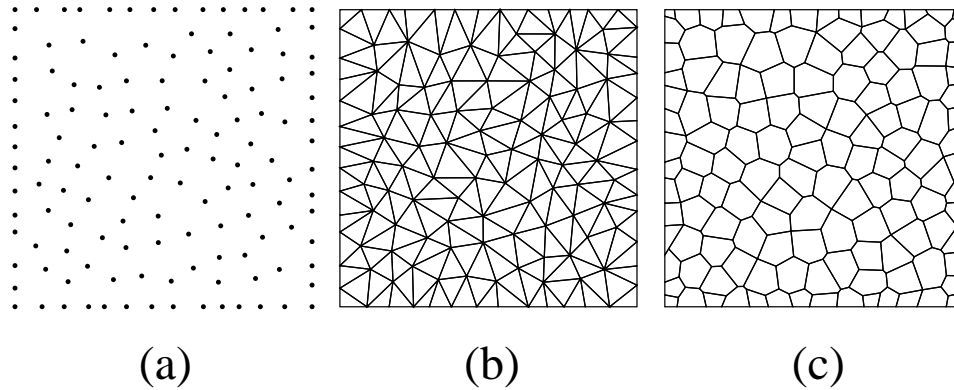


Figure 3. Process used to create the randomly close packed Voronoi tessellation: (a) random seeding until the theoretical maximum packing is reached with a constraint on minimum distance between points, (b) Delaunay triangulation, and (c) dual Voronoi tessellation.

In practice the RCP Voronoi tessellation can contain a number of relatively small edges. To regularize the mesh for use in explicit dynamics, these small features are simply deleted and the node pairs equivalenced in a recursive manner. Figure 4 shows the effect of this mesh regularization step on the Voronoi tessellation given in Figure 3. There is no discernable change in the tessellation. Histogram plots are also given showing the number of elements with a given number of edges both before and after the deletion of small edges. A majority of elements have six sides with all elements having in the range of four to eight sides after regularization.

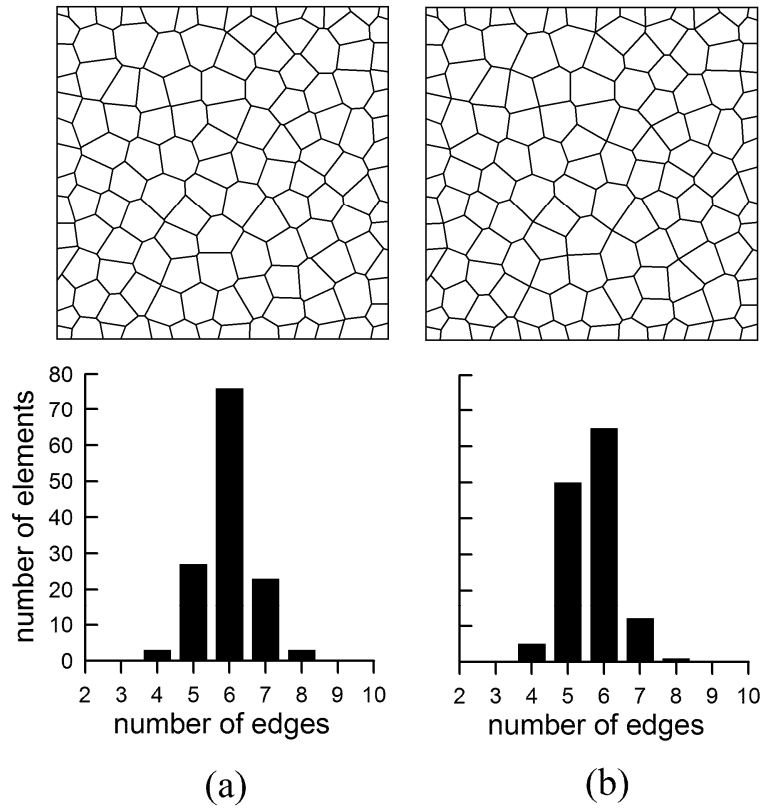


Figure 4. Regularization of the Voronoi tessellation by removing relatively small edges and equivalencing nodes: (a) raw Voronoi tessellation and (b) Voronoi mesh with constraint on minimum edge size. The histogram of the number of elements for a given number of edges is also given.

3. POLYHEDRAL ELEMENT FORMULATION

A general displacement based finite element formulation for plane faceted polyhedra applicable to large deformations has been achieved by Rashid [28] by developing *incompatible* polynomial based shape functions defined on the reference configuration that satisfy the minimum properties for convergence. Idelsohn, *et al* [29] used natural neighbor coordinates of a Delaunay tessellation of points to develop a ‘meshless’ finite element method. Wachspress [30] used perspective geometry concepts to develop rational shape functions on polyhedra. Sukumar [70] has developed a finite element formulation for *convex* polygons using shape functions defined on regular polygons. Ghosh [31–33] has developed polygonal elements based on the assumed-stress hybrid finite element method. An alternative polyhedral finite element formulation is introduced here. The reproducing kernel method [6] is used to generate *compatible* shape functions directly on the reference configuration. Since there is no mapping to a ‘parent’ element, the polyhedra can be *non-convex*. Thus, it is expected that these elements will be relatively robust under large deformations and large strain gradients. A functional comparison between these various approaches is being investigated. In the reproducing kernel method the nodal *shape* functions $\psi_I(\mathbf{x})$ are generated by first defining a nodal *weight* function $w_I(\mathbf{x})$ that has compact support, has a maximum value at the node, and is smoothly and monotonically decreasing away from the node. In typical meshfree applications the nodal weight functions are given circular supports in two dimensions and spherical supports in three dimensions. The nodal shape function is then defined as a spatial modulation of the nodal weight function,

$$\psi_I(\mathbf{x}) = C_I(\mathbf{x})w_I(\mathbf{x}) \quad (2)$$

where the nodal modulation function $C_I(\mathbf{x})$ is chosen so that $\psi_I(\mathbf{x})$ satisfies the desired reproducing and consistency requirements [3]. Let

$$\mathbf{g}^T(\mathbf{x}) = \{g_1(\mathbf{x}) \quad g_2(\mathbf{x}) \quad g_3(\mathbf{x}) \quad \cdots\} \quad (3)$$

be the vector of desired basis functions $g_i(\mathbf{x})$. For linear consistency $\mathbf{g}(\mathbf{x})$ is taken to be

$$\mathbf{g}^T(\mathbf{x}) = \{1 \quad x \quad y \quad z\} \quad (4)$$

Let N be the set of all nodes whose weight function support contains the location \mathbf{x} . The reproducing property of the shape function takes the form

$$\sum_{I \in N} \psi_I(\mathbf{x})\mathbf{g}(\mathbf{x}_I) = \mathbf{g}(\mathbf{x}) \quad (5)$$

In order to satisfy Eq. (5), $C_I(\mathbf{x})$ is taken to be of the form

$$C_I(\mathbf{x}) = \mathbf{a}^T(\mathbf{x}) \mathbf{g}(\mathbf{x} - \mathbf{x}_I) \quad (6)$$

where

$$\mathbf{a}^T(\mathbf{x}) = \{a_1(\mathbf{x}) \quad a_2(\mathbf{x}) \quad a_3(\mathbf{x}) \quad \dots\} \quad (7)$$

is a vector of unknown scalar valued functions $a_i(\mathbf{x})$. For linear consistency, substituting Eqs. (2) and (6) into Eq. (5) yields the matrix equation

$$\mathbf{A}(\mathbf{x}) \mathbf{a}^T(\mathbf{x}) = \{1 \quad 0 \quad 0 \quad 0\}^T \quad (8)$$

where $\mathbf{A}(\mathbf{x})$ is given by

$$\mathbf{A}(\mathbf{x}) = \sum_{J \in N} w_J(\mathbf{x} - \mathbf{x}_J) \bullet \begin{bmatrix} 1 & x - x_J & y - y_J & z - z_J \\ & (x - x_J)^2 & (x - x_J)(y - y_J) & (x - x_J)(z - z_J) \\ & & (y - y_J)^2 & (y - y_J)(z - z_J) \\ \text{sym} & & & (z - z_J)^2 \end{bmatrix} \quad (9)$$

Calculating the inverse of $\mathbf{A}(\mathbf{x})$ allows for the solution of the $a_i(\mathbf{x})$ in Eq. (7) and $C_I(\mathbf{x})$ in Eq. (6). The spatial derivatives of the shape functions can be calculated by direct differentiation of Eqs. (6), (8), and (9) [5]. By construction both the spatial coordinate \mathbf{x} and the displacement field \mathbf{u} are interpolated by the shape functions $\psi_I(\mathbf{x})$

$$\mathbf{x} = \sum_{I \in N} \psi_I(\mathbf{x}) \mathbf{x}_I, \quad \mathbf{u}(\mathbf{x}) = \sum_{I \in N} \psi_I(\mathbf{x}) \mathbf{u}_I \quad (10)$$

Thus, by definition this element formulation is isoparametric. Now consider the application of this general shape function construction to a Voronoi mesh. First, the nodal weight function is defined as follows. The compact support of node I is chosen to be the union of element domains attached to node I as with standard finite elements. Let this domain be denoted by Ω_I with boundary Γ_I and outward unit normal \mathbf{n} . The nodal weight function is defined as the solution to the following auxiliary Poisson problem,

$$\begin{aligned} \nabla^2 w + 1 &= 0 \quad \text{in } \Omega_I \\ w &= 0 \quad \text{on } \Gamma_I \cap \Gamma = \emptyset \\ \nabla w \cdot \mathbf{n} &= 0 \quad \text{on } \Gamma_I \cap \Gamma \neq \emptyset \end{aligned} \quad (11)$$

This auxiliary problem may be efficiently solved using standard boundary element techniques [34] to obtain the value of the weight function and its derivatives at the Voronoi cell integration points $\mathbf{x}_j, j = 1, \dots, M$, although in the two-dimensional example problem given in Section 6 the finite element method was used. Eqs. (2) through (11) can then be used to calculate the shape function $\psi_I(\mathbf{x})$. Note that by construction, $\psi_I(\mathbf{x}_j) = \delta_{IJ}$, and thus $\psi_I(\mathbf{x})$ satisfies the Kronecker

delta property. Also, along any edge there are only two supporting nodes. Therefore, the shape functions vary linearly along element edges. Thus, at least in two dimensions, these polyhedral finite elements are compatible with the standard first-order finite elements. For an example, the weight function and resulting shape function corresponding to an interior node of a regular hexagonal mesh is shown in Figure 5.

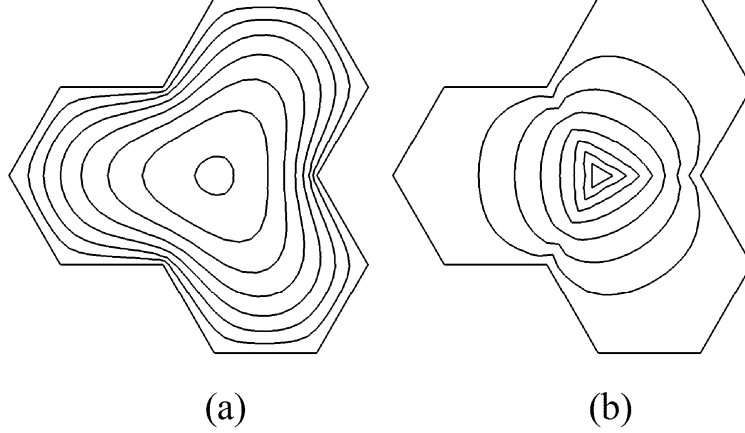


Figure 5. (a) Contour plot of the nodal weight function for an interior node of a regular hexagonal mesh. The weight function is obtained by solving the local boundary value problem defined by Eq. (11). (b) Contour plot of the shape function resulting from the application of the reproducing kernel methodology.

Note that the shape functions are defined directly on the undeformed configuration. There is no mapping to a ‘parent’ element. Thus, a total Lagrangian formulation of the governing equations is appropriate [35]. The conservation of linear momentum takes the form [5]

$$\text{DIV } \mathbf{P} + \rho_o \mathbf{f} = \rho_o \ddot{\mathbf{u}} \quad (12)$$

where \mathbf{f} is the body force vector per unit mass, \mathbf{u} is the displacement vector, ρ_o is the reference density, \mathbf{P} is the first Piola-Kirchhoff stress tensor,

$$\text{DIV } \mathbf{P} \equiv \nabla_o \mathbf{P} : \mathbf{I} = (\partial \mathbf{P} / \partial \mathbf{X}) : \mathbf{I} \quad (13)$$

\mathbf{I} is the identity tensor, and \mathbf{X} represents the position vector in the reference configuration. The weak form of Eq. (13) is given by

$$\int_{\Omega_o} \rho_o \ddot{\mathbf{u}} \cdot \delta \mathbf{u} \, dV = \int_{\Omega_o} \rho_o \mathbf{f} \cdot \delta \mathbf{u} \, dV - \int_{\Omega_o} \mathbf{P} : (\nabla_o \otimes \delta \mathbf{u}) \, dV + \int_{\Gamma_o} \mathbf{t}_o \cdot \delta \mathbf{u} \, dA \quad (14)$$

where Ω_o is the reference domain with boundary Γ_o , \mathbf{t}_o is the traction vector per unit initial area, and the displacement vector \mathbf{u} and the virtual displacement vector $\delta \mathbf{u}$ are members of the usual function spaces [35].

Rashid [28] has proposed a general methodology for developing Gauss points and their weights for integrating the weak form of the equilibrium equation for polyhedral elements. For the two-dimensional applications presented here, a reduced approach is adopted since each element domain is star shaped, and can be triangulated by connecting the element nodes to the element centroid. Standard Gauss rules for triangles are then applied. Chen [36] has noted that element formulations based on non-polynomial shape functions can result in a violation of the discrete form of Gauss's theorem (resulting from Gauss integration) with a subsequent reduction in accuracy and convergence rate. The shape functions formulated here are rational functions. For a given shape function ψ the continuous version of Gauss's theorem over an element subdomain Ω_e with boundary Γ_e and outward unit normal n_i is given by

$$\int_{\Omega_e} \psi_{,i} = \int_{\Gamma_e} \psi n_i \quad (15)$$

The discrete form is given by

$$\sum_j \omega_j \psi^j_{,i} = \sum_j \omega_j^\Gamma \psi^j n_i^j \quad (16)$$

where $\psi^j \equiv \psi(\mathbf{x}_j)$ and \mathbf{x}_j are the integration points with weights ω_j in the domain and ω_j^Γ on the element boundary. While Eq. (11) is a mathematical identity for any sufficiently smooth function, Eq. (12) does not in general hold. Herein, to maintain this identity the shape function derivatives at the integration points are modified by solving a linear programming problem based on the L_2 minimization of the difference of the shape function derivatives and their original values with Eq. (12) as a constraint. Typical corrections are on the order of only a few percent. These corrections are spatially local and do not require a global equation solution. Also, since a total Lagrangian formulation is used, the shape function derivatives are only corrected once, at the start of the analysis. Figure 6 shows the effect of this correction on the accuracy and convergence rate for a standard beam-bending verification problem [37] using a rectangular domain with an aspect ratio of 4.62 and a regular hexagonal mesh. Without the correction, the L_2 convergence rate in the displacement field is only 1.13. With the correction, the convergence rate is 1.88 which is close to the theoretical value of 2.0 for low order isoparametric elements.

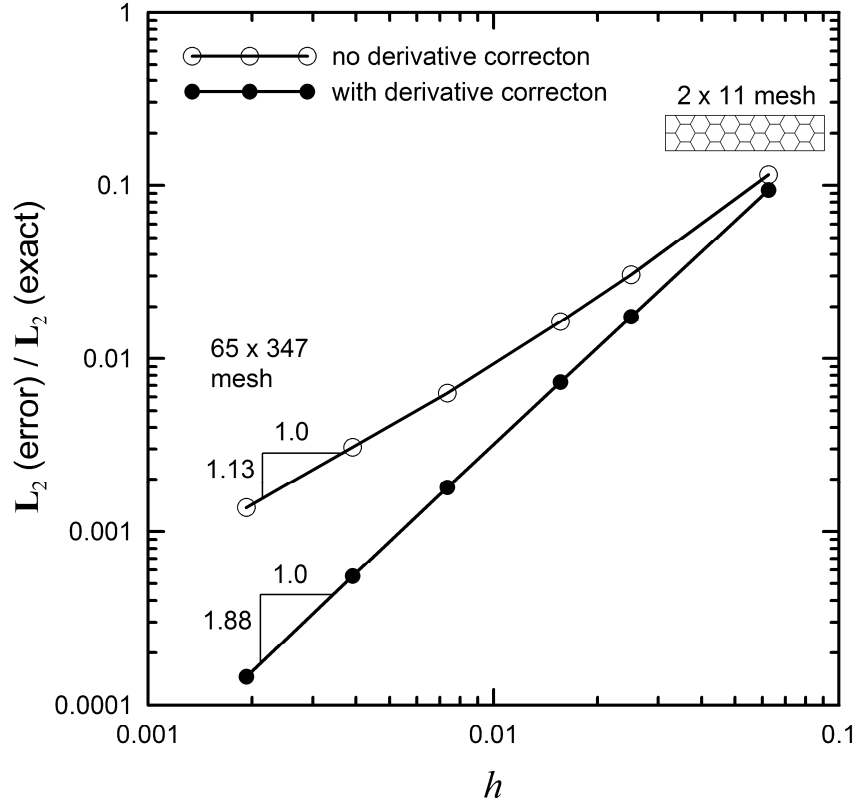


Figure 6. Effect of discrete integration consistency on the L_2 norm of the displacement error for the beam-bending verification problem using a regular hexagonal mesh with cell size h (plane stress, Poisson's ratio = 0.3, beam aspect ratio = 4.62).

Even though there is no mapping to a parent element in this element formulation, it is still expected that the robustness of these elements in large deformation analyses will be optimized when interior angles are maximized. Figure 7 shows the L_2 convergence rate in the displacement field for the beam-bending verification problem for two *random* perturbations of the regular hexagonal mesh. The normalized maximum perturbation for each mesh is denoted by r . There is only a slight sensitivity in the solution behavior to the initial shape of the elements. To handle incompressibility, a standard mean dilation formulation is used [28,38]. Figure 8 shows the effect of Poisson's ratio on the accuracy and convergence rate of the beam-bending verification problem for the case of plane strain. The mean dilation formulation essentially eliminates the typical locking behavior.

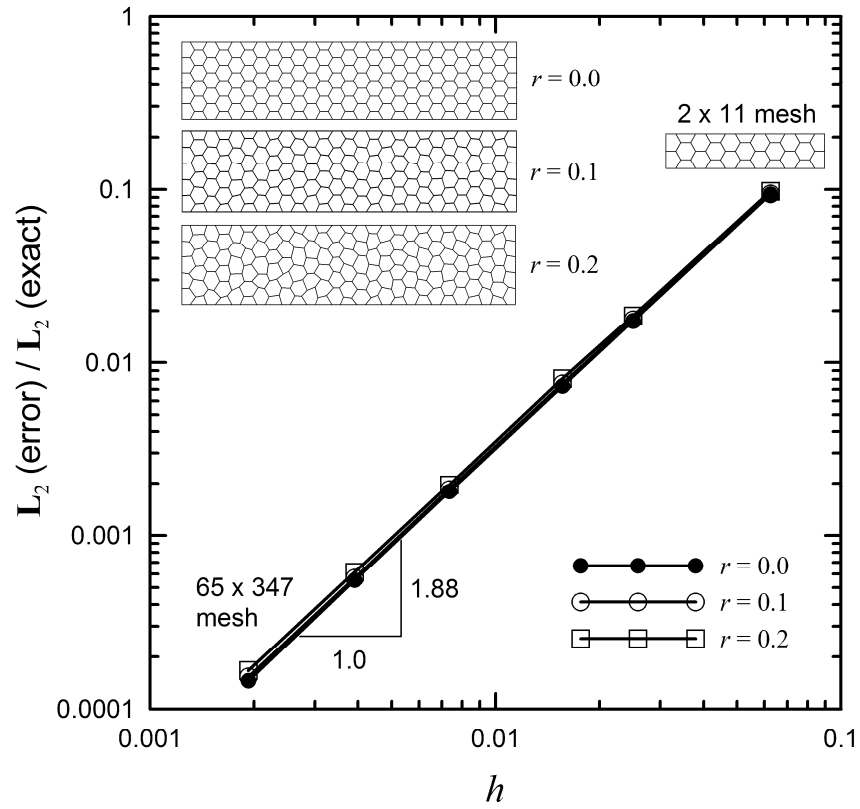


Figure 7. Sensitivity of the L_2 norm of the displacement error to perturbations in the regular hexagonal mesh for the beam-bending verification problem (plane stress, Poisson's ratio = 0.3).

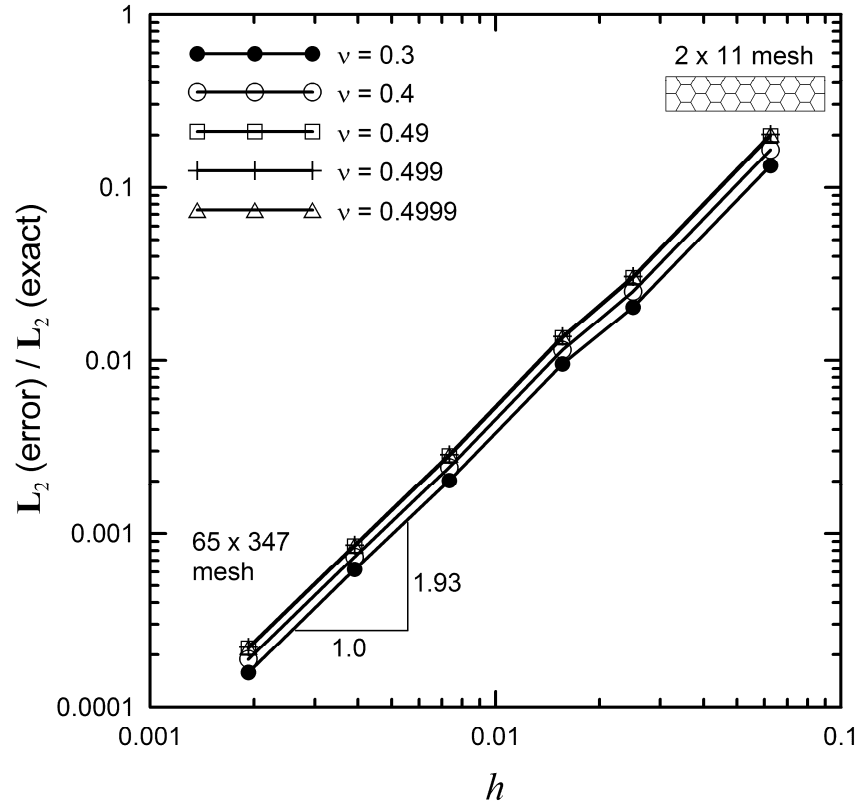


Figure 8. Effect of Poisson's ratio on the L_2 norm of the displacement error for the beam-bending verification problem using a mean dilation formulation and a distorted hexagonal mesh ($r = 0.2$, plane strain).

In the results presented so far each element has been integrated by triangulating the element and using standard three-point Gauss integration for each triangle. Since each element is star shaped the triangulation is obtained simply by connecting the element centroid with each element node. Figure 9 shows the effect of the number of integration points on the accuracy and convergence rate of the beam-bending verification problem for the case of plane stress. The use of a minimum number of integration points (while avoiding zero-energy modes) results in increased accuracy for the plane stress case. The plane strain case exhibited an opposite effect.

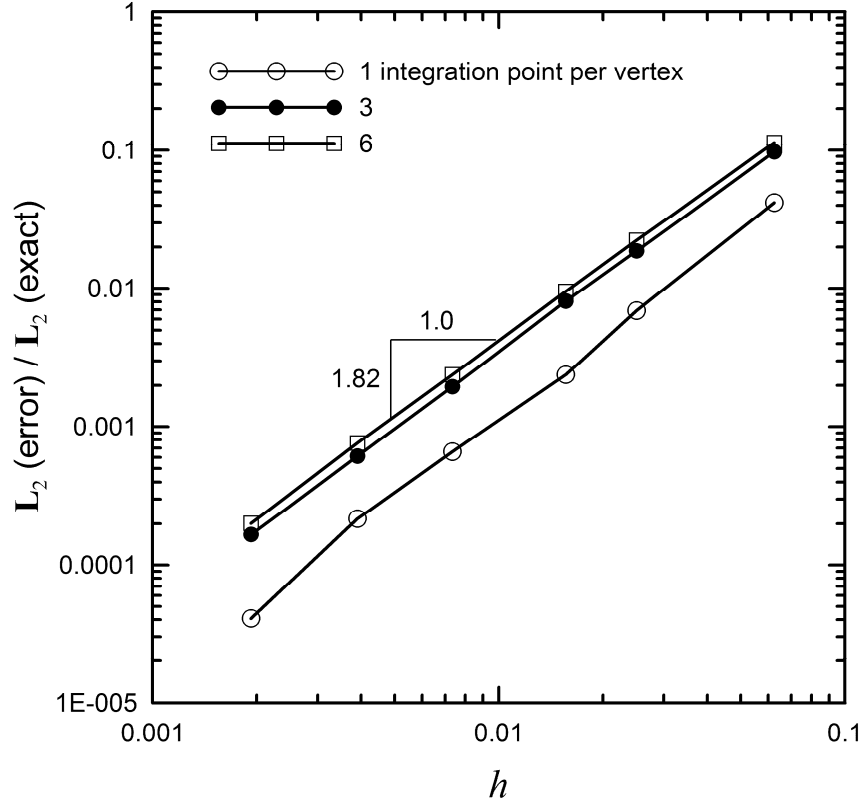


Figure 9. Effect of number of element integration points on the L_2 norm of the displacement error for the beam-bending verification problem using a distorted hexagonal mesh ($r = 0.2$, plane stress).

An explicit dynamics central difference time integration scheme [39] is used to integrate the semi-discrete equations resulting from Eq. (14). The mass matrix is diagonalized using the ‘special lumping technique’ of Hinton [40] as it always produces positive lumped masses. This mass lumping procedure is recommended by Hughes for non-standard element formulations [41].

4. DYNAMIC MESH CONNECTIVITY AND CONTACT

Since the generation of one or more new fracture surfaces (faces in three dimensions and edges in two dimensions) can occur every time step, an efficient algorithm and data structure is needed to update the mesh connectivity as these surfaces nucleate. The possible algorithms may be partitioned into two paradigms: (1) 'top-down' modification and (2) 'bottom-up' modification. A top-down algorithm attempts to locally modify the mesh connectivity while minimizing the overall change to the underlying data structure and may be recursive in nature (see, for example, [12]). Alternatively, a bottom-up algorithm assumes that there are a large number of new crack faces per time step. The initial connectivity is completely discarded and recreated using the new fracture state. Top-down modifying algorithms are very efficient when there are a small number of new crack faces, but their implementation is somewhat involved. Herein, a bottom-up modification algorithm is used. At the beginning of the connectivity update process all elements are taken to be disconnected with unique nodes. Let the ordered pair (a, i) represent the i th node of the a th element. An equivalence relation [42] is defined on the set of element nodes such that (a, i) and (b, j) are equivalent if they are directly connected across an uncracked face (3D) or edge (2D). This equivalence relation is used to partition the set of all element nodes into equivalence classes [42]. At the end of the connectivity update process a new global node is created for each equivalence class. The position and velocity of the old global nodes are then copied into the new definitions. The partition of the element nodes requires only a single pass through all face pairs. The partition is initialized by taking each element node to be a unique mathematical set. During the pass through the list of face pairs, sets are united using the criterion described above. The final collection of sets constitutes the partition. This methodology has proven to be simple, robust, and free of 'special cases.' Note that for crack *initiation* in the *interior* of a body, at least two cracked edges are needed to realize a change in the mesh connectivity in two dimensions while at least three faces are needed in three dimensions. For crack *initiation* on the *boundary* of a body, only one cracked edge is needed to realize a change in the mesh connectivity in two dimensions while at least two faces are needed in three dimensions.

By its nature, pervasive failure involves a large amount of self-contact. It is thus essential to have a simple and robust contact algorithm, free of 'special cases.' To avoid any constraints on surface topology that is typical of master/slave contact algorithms, a simple penalty approach is adopted here. Each polyhedral element on the instantaneous surface of the domain is treated independently and checked for mutual penetration as in the discrete element method [43]. Let C represent the set of elements on the instantaneous surface of the domain. At the start of the simulation C is initialized with all elements on the surface of the reference domain. As the simulation progresses and new crack surfaces nucleate, elements previously on the interior that are now on the boundary are added to C . Thus, the size of C is monotonically increasing during the simulation. In the contact search phase the elements in the set C are spatially sorted onto an overlaid rectangular grid based upon minimal bounding boxes. All element pairs that are 'close' are then checked for mutual penetration. If penetration is detected, a penalty force based on both the penetrating velocity and penetration is applied following Heinstein [44]. The velocity based penalty parameter was chosen to obtain 'plastic' impact conditions. The displacement based penalty parameter was chosen to be as small as possible yet still prevent gross penetration under quiescent conditions, recognizing the fact that the critical time step can be adversely affected by

too large a value. The use of spatial sorting is very efficient. Since there are no comparisons required between elements to populate the overlay grid, the sorting process is order N complexity where N is the number of elements in the contact set C . If the cell size of the overlay grid is taken to be the characteristic element size, each grid cell is guaranteed to have only a few elements in each cell due to the interpenetration constraint.

5. LIMITS OF PREDICTABILITY AND CONVERGENCE

An overriding goal in computational mechanics is to be ‘predictive.’ However, in the field of nonlinear dynamics it is now well known that there exist many deterministic systems that are inherently unpredictable¹ beyond a certain critical time, the so called predictability horizon [45, 65]. A common example is provided by the game of billiards in which a ball is given an initial velocity and trajectory with the goal of striking a series of balls arrayed on a table. Due to extreme sensitivity in initial conditions it is virtually impossible to strike more than three or four balls in succession. Such problems exhibit an exponential growth in time of small variations in the initial conditions and therefore possess an inherent predictability limit in time [45]. To see this let $\mathbf{x}(t)$ represent a trajectory in phase space (a solution for a given set of initial conditions) for a dynamical system. Let $\mathbf{x}(t) + \delta(t)$ represent a slightly different trajectory in which the initial conditions are varied by a very small amount δ_0 . The difference in the two trajectories $\delta(t)$ can be described by the relation

$$\|\delta(t)\| \sim \|\delta_0\| e^{\lambda t} \quad (17)$$

where λ is the Liapunov exponent. If λ is positive then the predictability horizon is given by [45]

$$t_{\text{horizon}} \sim O\left(\frac{1}{\lambda} \ln \frac{a}{\|\delta_0\|}\right) \quad (18)$$

where a represents an acceptable accuracy with respect to the ‘true’ trajectory $\mathbf{x}(t)$ and $a > \|\delta_0\|$. The logarithmic dependence on $\|\delta_0\|$ defeats any hope of long term system predictability. For example suppose an acceptable accuracy in the model prediction is 10% ($a = 10^{-1}$) and the precision in the initial conditions is $\|\delta_0\| = 10^{-3}$. From Eq. (18), $t_{\text{horizon}} \approx 2(\ln 10)/\lambda$. If the precision in the initial conditions is increased to 10^{-6} then $t_{\text{horizon}} \approx 5(\ln 10)/\lambda$. Thus, increasing the precision in the initial conditions by three orders of magnitude only increases the predictability horizon by a factor of 2.5. For linear systems the predictability horizon is infinite. For stochastic systems (nondeterministic) the predictability horizon is zero.

Sensitivity to initial conditions is one necessary condition for chaos [45]. Chaotic behavior is actually quite prevalent in mechanical systems that undergo intermittent impact [66], for example a bouncing ball on a vibrating table [67]. Due to the extensive interactions among advancing cracks and ubiquitous self contact-impact, pervasive failure problems are extremely sensitive to initial conditions (in addition to system parameters) as well and thus exhibit a finite predictability horizon. This will be demonstrated in the examples given in Sections 6 and 7. However, unlike fully chaotic dynamical systems, pervasive failure processes are of finite duration and thus experience only short-term ‘transient chaos.’ Also, certain quantities of interest may be more predictable than others. Global quantities such as dissipated energy, depth

¹ Here, a dynamical system is considered predictable if given a specified initial state of the system to relative accuracy ε the state of the system at a later time can be specified to within an accuracy of at least order ε .

of penetration, and the ballistic limit are expected to be more predictable than local quantities such as fracture paths.

Beyond the predictability horizon it is more appropriate to describe the dynamic system behavior using statistical theory even though the governing equations are completely deterministic. For a dynamical system exhibiting long-term chaotic behavior the statistical properties can be obtained by merely sampling one simulation over a long time interval. For pervasive failure processes exhibiting short-term transient chaos the statistical properties of the system can be obtained using an ensemble of simulations that are ‘seeded’ with small initial random variations in initial conditions or system parameters such as geometric imperfections and material properties. Furthermore, due to the transient chaotic behavior, conventional definitions of convergence with respect to mesh refinement are no longer applicable beyond the predictability horizon. Instead, more general notions of convergence are necessary, ones based on statistical theory or measure theory in analysis. The following three definitions of convergence are adapted from statistical theory [46] for the particular case of convergence with respect to mesh refinement: *convergence in distribution*, *convergence in probability*, *convergence in r -th mean*. They are given in order of increasing ‘strength’ in the sense that if a sequence of probability distributions converge in probability then it also converges in distribution, and if a sequence of probability distributions converge in r -th mean then in also converges in probability [46]. Let $P_h(\mathbf{q})$ represent the probability distribution of a quantity of interest \mathbf{q} at a specific time during a pervasive failure simulation for a given mesh resolution h . Let F_h be the cumulative distribution function of P_h . Convergence in distribution is defined as

$$\lim_{h \rightarrow 0} F_h(\mathbf{q}) = F(\mathbf{q}) \quad (19)$$

For example suppose that the quantity of interest \mathbf{q} is the maximum crack length, a scalar. For a given mesh resolution h the probability distribution $P_h(l)$ represents the probability that the maximum crack length is l . The probability that the maximum crack length is less than L is given by $F_h(L)$. For convergence in distribution the sequence $F_h(L)$ must converge for each crack length L . *Convergence in probability* is defined as

$$\lim_{h \rightarrow 0} \Pr(P_h(\mathbf{q}) - P(\mathbf{q}) > \varepsilon) = 0 \quad (20)$$

for every $\varepsilon > 0$. Here $\Pr(P_h(\mathbf{q}) - P(\mathbf{q}) > \varepsilon)$ represents the probability that $P_h(\mathbf{q})$ is outside a tolerance ε of $P(\mathbf{q})$. *Convergence in the r -th mean* ($r \geq 1$) is defined as

$$\lim_{h \rightarrow 0} E\left(|P_h(\mathbf{q}) - P(\mathbf{q})|^r\right) = 0 \quad (21)$$

where E represents the expected value. For $r = 1$ this represents *convergence in mean*, and for $r = 2$ this is *convergence in mean square*. Note that the quantity of interest \mathbf{q} may itself be a probability distribution, e.g. a fragment mass distribution, or a moment of a probability distribution such as the mean fragment mass. Also note that the above definition of convergence *in mean* is fundamentally different than convergence *of the mean*.

For a given pervasive failure problem a computational demonstration of convergence in these measures could necessitate thousands of simulations at each level of mesh refinement. Such Monte Carlo analyses would be difficult for large scale three-dimensional problems. The situation is further complicated by the fact that the use of interelement cohesive based finite element simulations is predicated on a mesh resolution that is finer than the cohesive zone size. For many material systems, such as brittle ceramics, the cohesive zone size is relatively small and can be computationally expensive to resolve. Recently, Molinari [68] has performed a detailed investigation into the convergence behavior of the total dissipated cohesive energy for a fragmenting ceramic ring in a one dimensional setting using a random mesh. Extremely fine meshes were needed to demonstrate convergence in the mean value. Resolving a full probability distribution would be even more difficult. In the following pervasive failure example only a small ensemble of simulations are performed with the modest goal of merely highlighting the large variation in results and extreme sensitivity to initial conditions. Future work will focus on quantitative demonstrations of convergence using the statistical measures given in Eqs. (19–21).

6. EXAMPLE

A two-dimensional explicit dynamics program implementing the RCP Voronoi methodology with dynamic mesh connectivity was written using the C++ programming language. The object-oriented functionality available in C++ facilitated the implementation. The C++ Standard Template Library, providing the set, vector, list, and map dynamic data structures was particularly useful [47]. A three dimensional *parallel* implementation seems challenging due to the extensive modifications in the mesh topology and the necessary processor load rebalancing. It is envisioned that the project *phdMesh* (parallel, heterogeneous, and dynamic unstructured meshes) [48] will provide a convenient platform for developing a 3D parallel implementation.

For an example consider a low-strength concrete column (0.3 m by 1.83 m) impacting a rigid plane at a striking velocity of 7.6 m/s and 45° angle of obliquity as shown in Figure 10. The column is idealized as a two-dimensional plane strain structure composed of a linear elastic material (Young's modulus $E = 28.3$ GPa, Poisson's ratio $\nu = 0.2$, density = 2.25 g/cm³) with a Mohr-Coulomb localization criterion with a tensile cutoff σ_o as shown in Figure 11. The Mohr-Coulomb failure criterion is given by

$$|\tau| = c - \mu\sigma \quad (22)$$

where τ is the limiting shear stress on a plane, σ is the normal stress on the same plane, c is the cohesion, and μ is the coefficient of internal friction. For this example, $c = \sigma_o = 3.7$ MPa and $\mu = 0.75$. The cohesive traction model follows that of Camacho and Ortiz [15]. The cohesive parameters presented in reference [50] for mortar are used with an overall fracture energy $G = 57$ J/m². An estimate of the cohesive zone length can be obtained using an equivalent linear elastic fracture mechanics model in which the length of the cohesive zone L is given by $L = k l_{ch}$ where $l_{ch} = E'G/\sigma_o^2$ is Hillerborg's characteristic size, $E' = E/(1-\nu^2)$, and k is a dimensionless constant in the range 2 to 5 [49, 69]. Using the above material values gives $l_{ch} = 0.12$ m and a minimum value for L of 0.25 m. This value for the cohesive zone length is roughly equal to the thickness of the concrete column in the present example. In order to detect if the localization criterion (Eq. 22) has been obtained at an interelement face, the stress field is interpolated from the integration points of the two attached elements. Once the localization criterion is met at an interelement face, the connectivity of the finite element mesh is updated as described in Section 4, and the cohesive traction is invoked. The normal tractions are taken to be zero under over-closure. The contact algorithm is used to prevent interelement penetration.

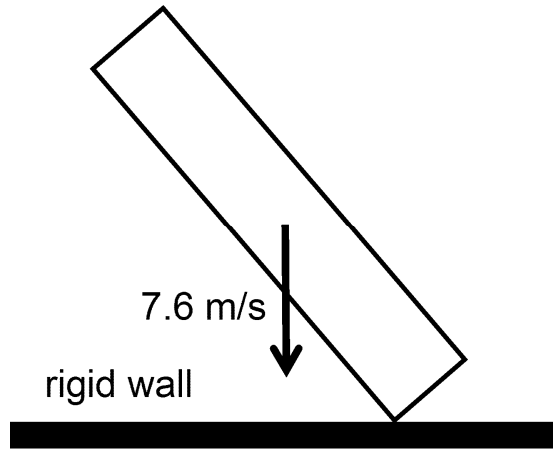


Figure 10. A low strength concrete column striking a rigid wall at a 45 degree angle.

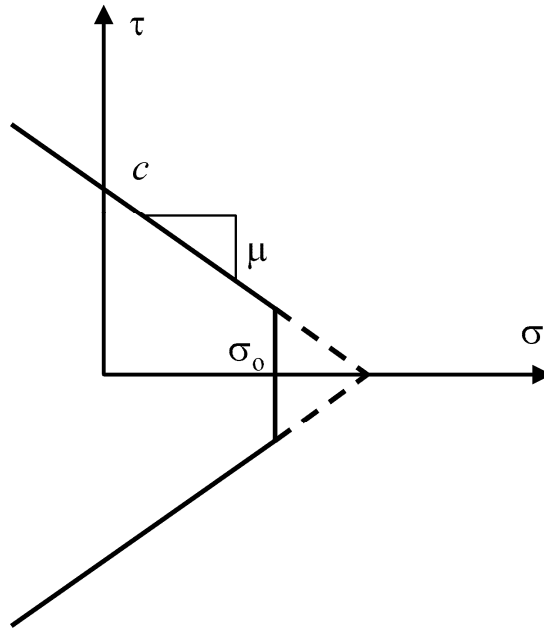


Figure 11. Mohr-Coulomb failure surface in shear (τ) normal-stress (σ) space, with cohesion c , tensile cutoff σ_0 , and internal friction μ .

For the results and discussion to follow, the i th realization of a RCP Voronoi tessellation with a characteristic cell size h will be denoted R_i^h . Four characteristic cell sizes will be considered, 8.0, 4.0, 2.0, and 1.0, with $h = 1.0$ corresponding to a physical dimension of 0.635 cm. Three realizations of the RCP Voronoi mesh are shown in Figure 12 for $h = 8.0$, $h = 4.0$, and $h = 2.0$. Figure 13 shows a series of snapshots in time of the concrete column during the impact event using the $R_i^{2.0}$ mesh. In addition to the boundary, fracture surfaces whose cohesive tractions have fully softened are also shown. There is extensive fragmentation at the impact corner. Note the bending induced fracture at the midsection involving crack coalescence and branching. There is additional fragmentation after the column rotates and the rear section strikes the rigid plane at approximately 200 ms. The fragmentation process is essentially complete by 300 ms.

To illustrate the extreme sensitivity to initial conditions, the simulation was rerun with an initial striking angle of 44.99° , only a 0.02% difference. The simulation results are shown in Figure 14. Note that the fracture and fragmentation results are qualitatively similar but distinctly different with respect to specific cracks and resulting fragment sizes. As described in Section 5, due to the extreme sensitivity in initial conditions of this problem it is expected to be very difficult to demonstrate mesh convergence in a classical sense.

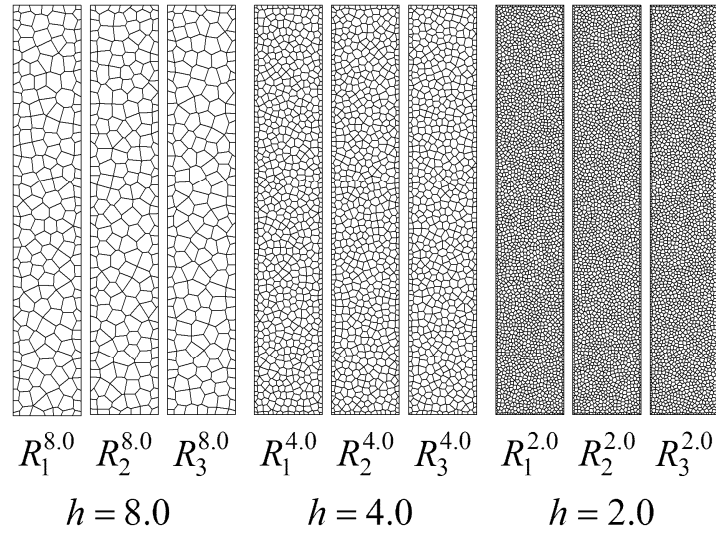


Figure 12. Randomly close packed Voronoi realizations for three different characteristic cell sizes, $h = 8.0$, $h = 4.0$, and $h = 2.0$. Three realizations are shown for each characteristic cell size.

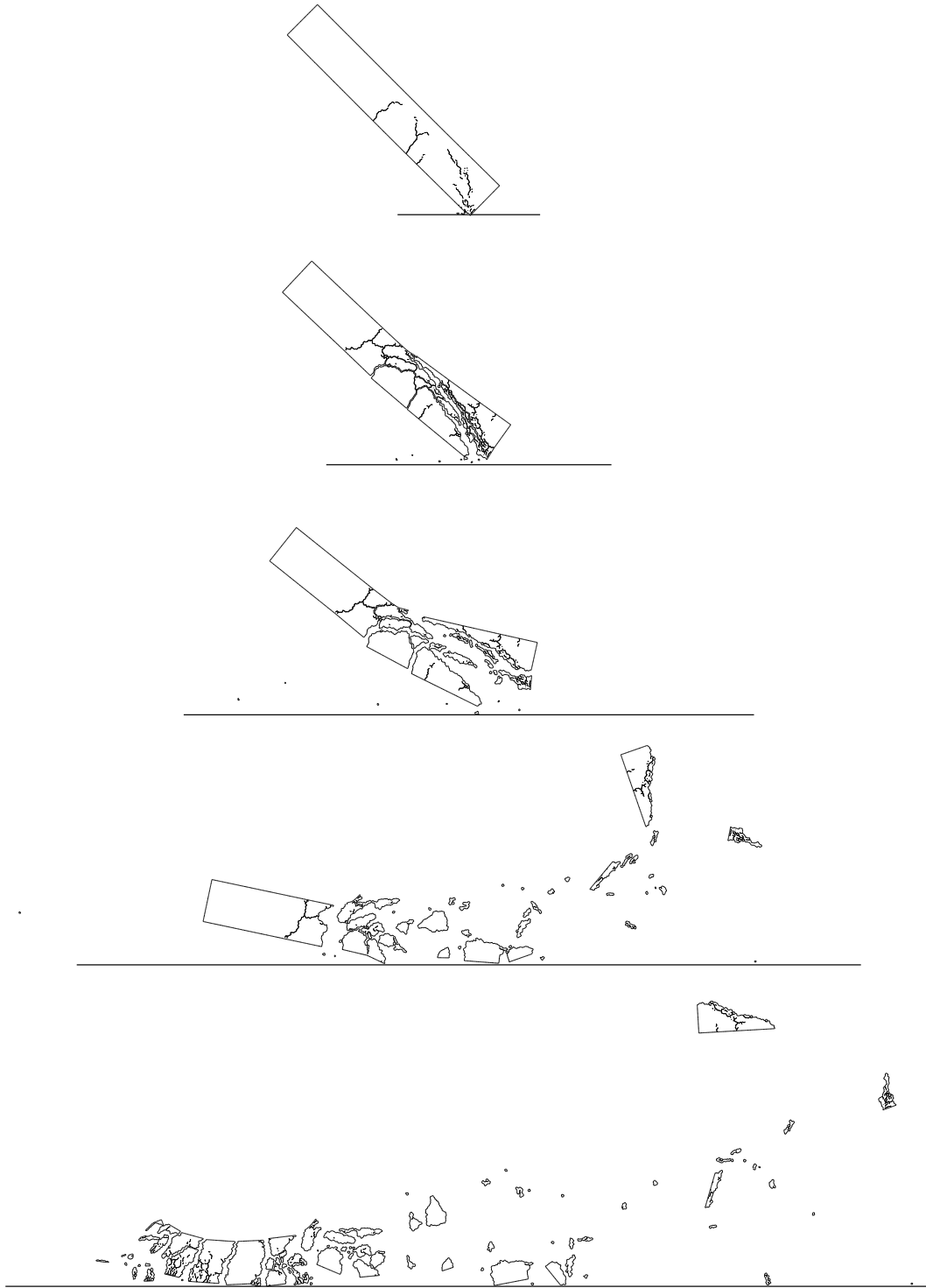


Figure 13. Deformed state and crack surfaces of the concrete column at a number of instances in time after impact with an impact angle of 45.00° ($R_1^{2.0}$ mesh). Only cracks that have fully softened (no cohesive tractions) are shown. Impact times are 2, 10, 30, 150, and 230 ms.

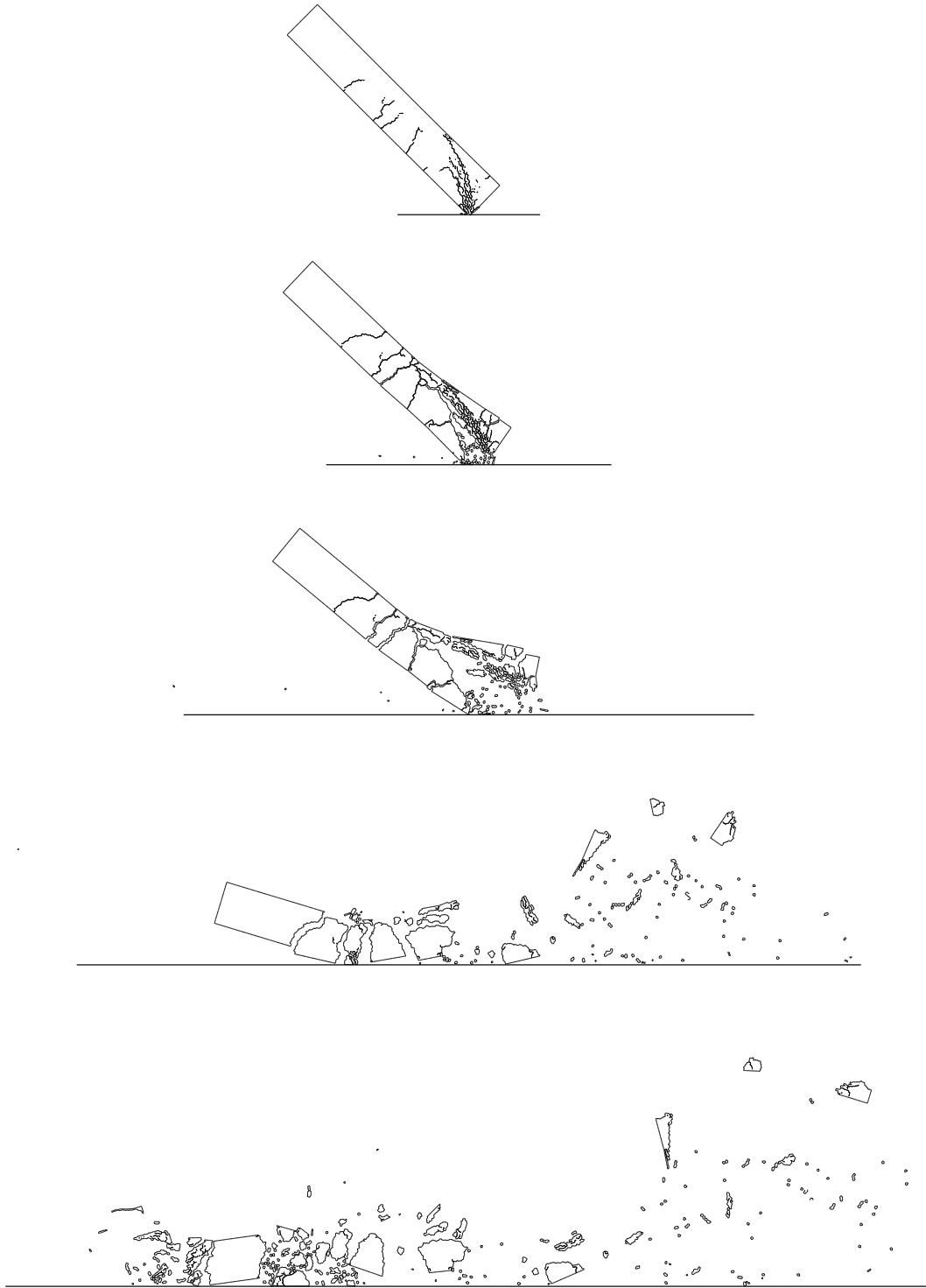


Figure 14. Deformed state and crack surfaces of the concrete column at a number of instances in time after impact with an impact angle of 49.99° ($R_1^{2.0}$ mesh). Only cracks that have fully softened (no cohesive tractions) are shown. Impact times are 2, 10, 30, 150, and 230 ms.

There are a number of physical sources of variability that could be included in the initial conditions and model parameters to induce a distribution in the physical response. One important source of variability is the material properties. Ideally, a correlated random field representation of the material properties, including localization, would be included in the analysis. If the body is idealized as homogenous, then the random orientation of the RCP Voronoi structure provides in effect a non-physically based variation in the localization properties of the material. Performing multiple simulations with different RCP Voronoi realizations will result in a distribution of any nonconserved quantity. Since in general the distribution will not be uniform, each specific simulation produces a different value. Thus, *only the distribution itself can be regarded as 'mesh independent'*. Suppose the engineering quantity of interest is the cumulative distribution of fragment mass fraction. The cumulative distribution of fragment size at the simulation time of 300 ms is shown in Figure 15 for twelve RCP Voronoi realizations $R_i^{2.0}$, $i \in \{1,2,3,\dots,12\}$ using homogeneous material properties. Note that each distribution is distinctly different. The maximum fragment size for a given simulation may be identified by the last 'step' in the curve. To demonstrate the sensitivity to material property variations, the impact simulation for the $R_i^{2.0}$ mesh was performed with a $\pm 5\%$ uniform variation in elastic modulus and the internal friction μ . Twelve realizations of material properties were produced. The resulting cumulative distributions in fragment mass fraction are shown in Figure 16. The cumulative distribution for the homogenous case is also given. Note that the variability between the cumulative distributions is similar to the variability for the multiple mesh realizations but with homogenous material properties.

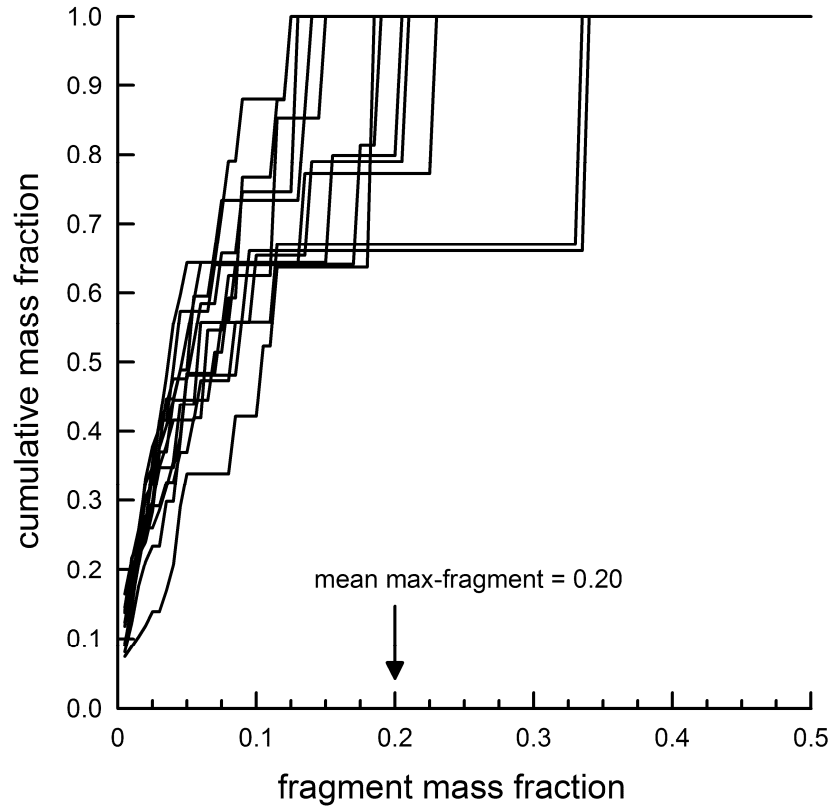


Figure 15. Cumulative distribution of the fragment mass-fraction at a simulation time of 300 ms for the $R_i^{2,0}$, $i \in \{1,2,3,\dots,12\}$ RCP Voronoi mesh family with homogeneous material properties. The mean of the *maximum*-fragment mass-fraction is denoted by the arrow.

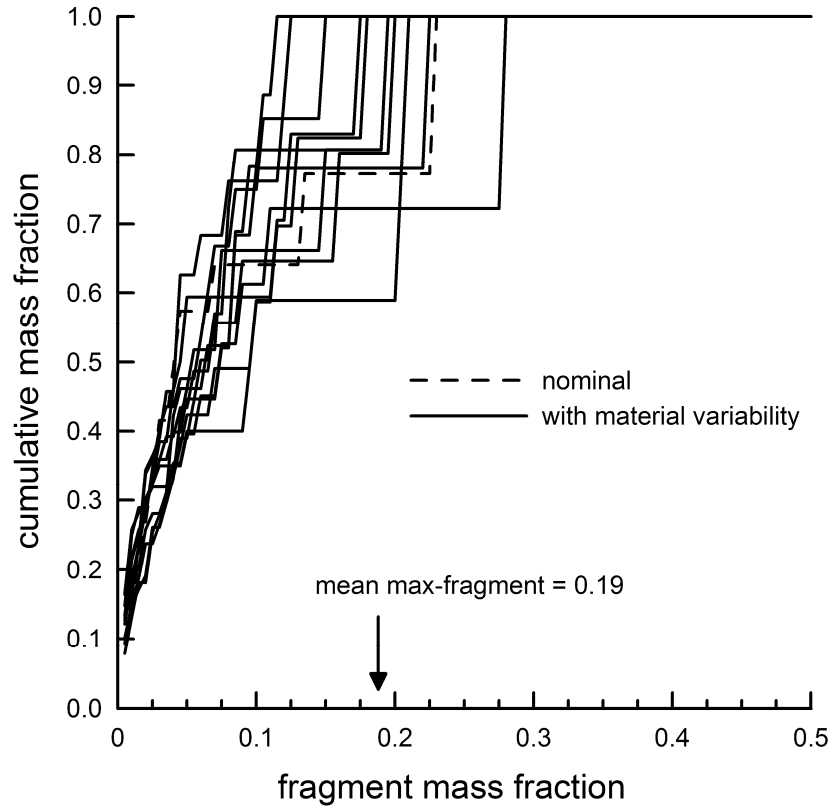


Figure 16. Cumulative distribution of the fragment mass-fraction at a simulation time of 300 ms using the $R_1^{2.0}$ mesh with twelve material realizations of a $\pm 5\%$ uniform variation on elastic modulus and Mohr-Coulomb failure surface. The homogenous material case is given for comparison.

The corresponding cumulative distributions for the $R_i^{8.0}$, $R_i^{4.0}$, and $R_i^{1.0}$ mesh families using homogeneous material properties are shown in Figure 17, Figure 18, and Figure 19, respectively. In addition, the maximum fragment size for each mesh realization and refinement level is given in Figure 20. The convergence of the distribution of cumulative distributions is not apparent, although twelve realizations is a very small sample size for what is expected to be a complex statistical distribution for fragment size. As noted in Section 5 a definitive demonstration of convergence could necessitate thousands of such simulations.

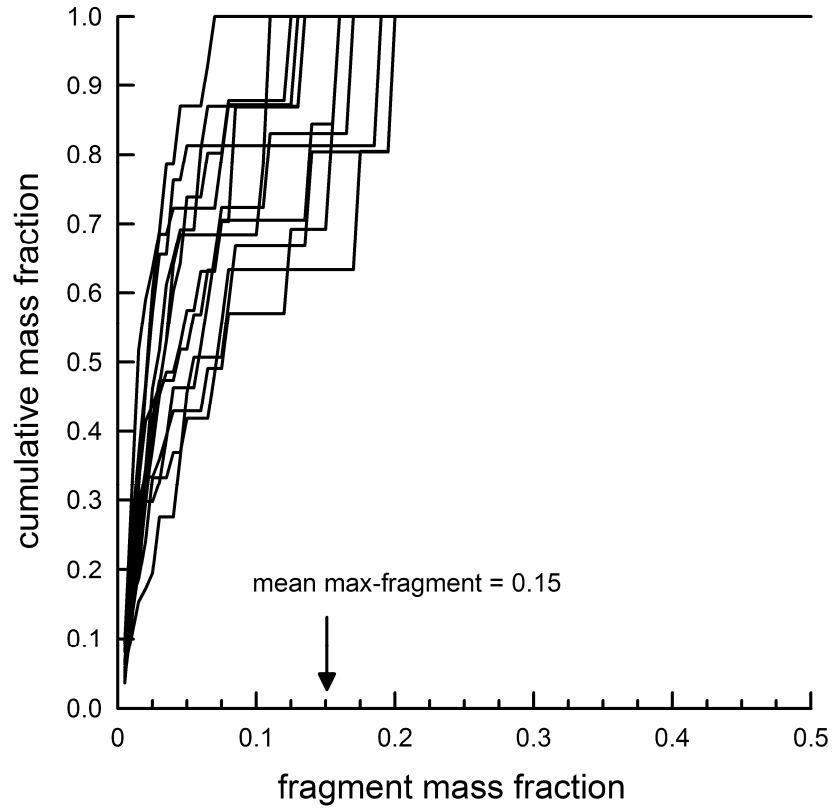


Figure 17. Cumulative distribution of the fragment mass-fraction at a simulation time of 300 ms for the $R_i^{8,0}$, $i \in \{1,2,3,\dots,12\}$ RCP Voronoi mesh family with homogeneous material properties. The mean of the *maximum*-fragment mass-fraction is denoted by the arrow.

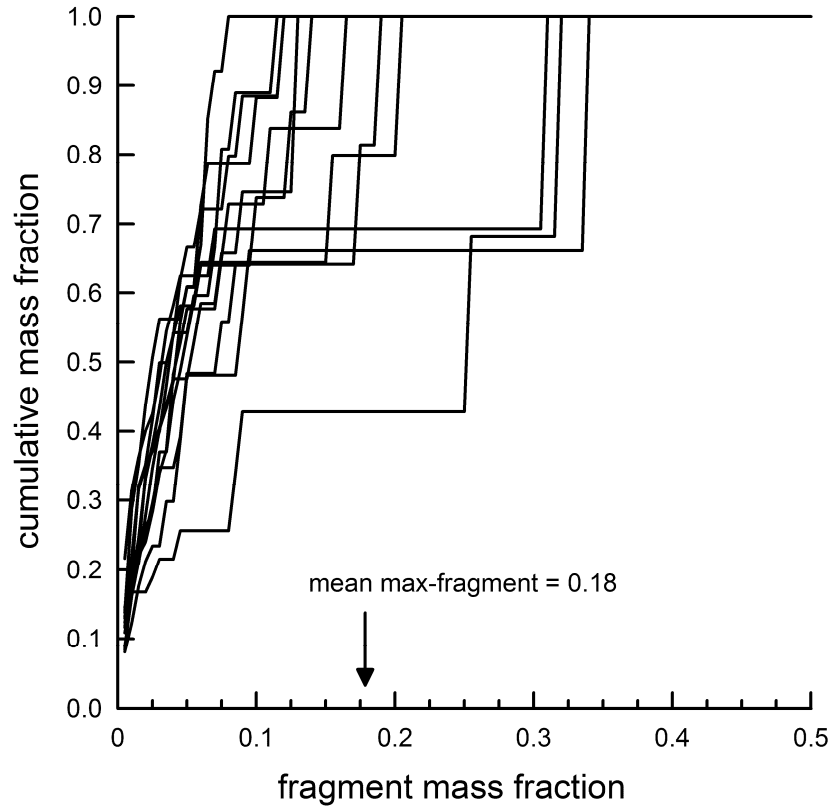


Figure 18. Cumulative distribution of the fragment mass-fraction at a simulation time of 300 ms for the $R_i^{4,0}$, $i \in \{1,2,3,\dots,12\}$ RCP Voronoi mesh family with homogeneous material properties. The mean of the *maximum*-fragment mass-fraction is denoted by the arrow.

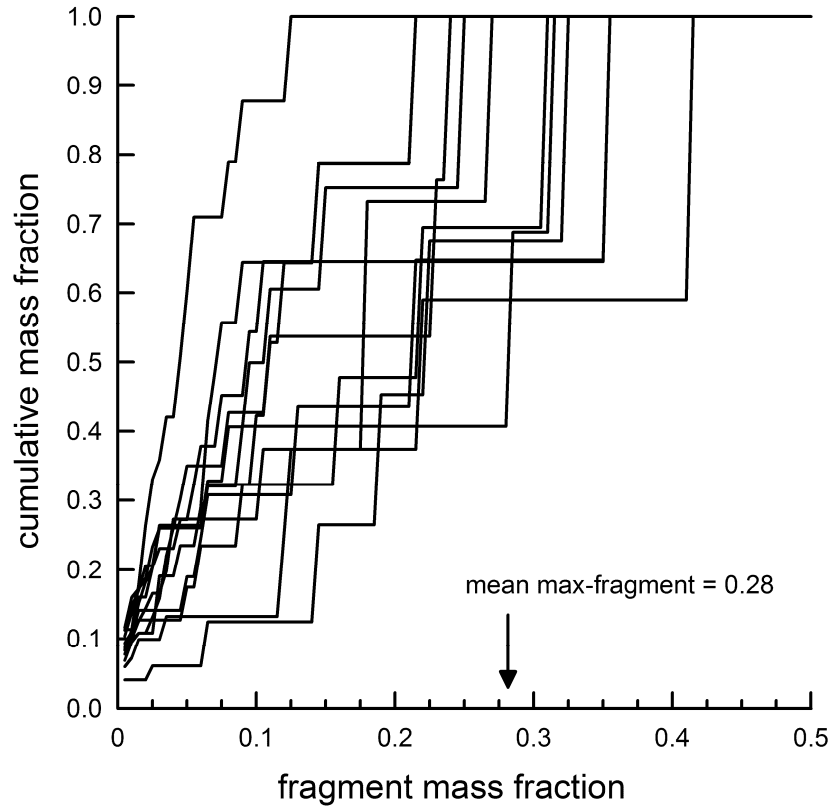


Figure 19. Cumulative distribution of the fragment mass-fraction at a simulation time of 300 ms for the $R_i^{1.0}$, $i \in \{1,2,3,\dots,12\}$ RCP Voronoi mesh family with homogeneous material properties. The mean of the *maximum*-fragment mass-fraction is denoted by the arrow.

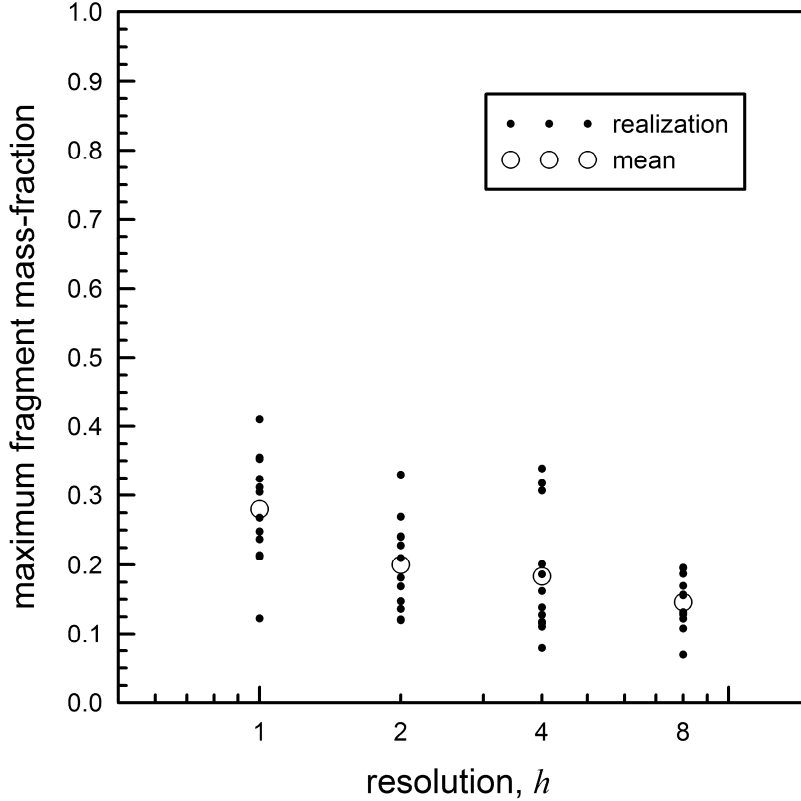


Figure 20. The *maximum* fragment size for twelve RCP Voronoi mesh realizations at four mesh resolutions $R_i^{8.0}$, $R_i^{4.0}$, $R_i^{2.0}$, and $R_i^{1.0}$ with homogeneous material properties. For each mesh resolution the mean of the maximum fragment mass-fraction is also given.

An additional consideration arises with the use of bulk constitutive models that include internal state variables for representing continuum damage from microcracking. The presented computational methodology provides an *explicit* representation of macroscopic cracks. Conversely, continuum damage mechanics provides an *implicit* homogenized representation of microcracks. As an RCP Voronoi mesh is refined to smaller scales the question of self-consistency between the explicit macroscopic representation of cracks and the implicit homogenized representation comes into question. This notion of self-consistency and scale dependence is a central theme in fractal geometry descriptions of materials [51–54], and is important for understanding the size effect in quasi-brittle materials [49, 55].

7. DISCRETE FRACTURE ABSTRACTIONS

A few advantages of representing fracture surfaces by discrete facets were discussed in Section 1. A discrete fracture representation also enables additional levels of mathematical abstraction that can be useful, for example, in comparing multiple simulations using the same RCP Voronoi mesh. In this section a few of these abstractions are proposed and briefly demonstrated.

7.1 fracture state space

Consider a given RCP Voronoi mesh with N internal faces. At a high level of abstraction the fracture state of a given face may be described as either uncracked (0) or cracked (1). If the set of all faces is enumerated from 1 to N , the fracture state of the entire body is described by the sequence $(a_1, a_2, a_3, \dots, a_N)$ where each a_i is either 0 or 1 . The set of all such binary sequences forms a fracture state space denoted by E^h . The size of E^h is finite and is given by 2^N . While finite, the space is quite large. (For example, the $R_i^{8.0}$ mesh shown in Figure 12 has 490 internal edges, and the size of E^h is $2^{490} \cong 10^{148}$. The $R_i^{4.0}$ mesh has 1847 internal edges, and the size of E^h is approximately $2^{1847} \cong 10^{556}$.) Now let X_i represent a crack state at a given time t_i in an explicit dynamics simulation. The sequence $(X_i)_{i \geq 0}$, defines the fracture history or process. Many other fracture state spaces could be defined as well. For example, if the fracture state is described by the sequence $(a_1, a_2, a_3, \dots, a_N)$ where each a_i is now a real number representing the crack face opening displacement (cfod) of face i , the set of all such sequences forms a new fracture state space denoted by F^h .

A metric space [56] is a set X and a distance function d defined on X , such that for all $x, y, z \in X$, the following four axioms hold: (1) d is real valued, finite, and nonnegative, (2) $d(x, y) = 0$ if and only if $x = y$, (3) $d(x, y) = d(y, x)$, and (4) $d(x, y) \leq d(x, z) + d(z, y)$. For the fracture state space E^h one possible distance function is the Hamming distance [57] used in coding and information theory. In this case the Hamming distance function $d_H(x, y)$, $x, y \in E^h$ is defined as the number of faces that have different fracture states (0 or 1). Armed with this metric the distance between two fracture states can be calculated either at different times during one simulation or between two distinct simulations using a specific RCP Voronoi mesh. Note that for a specific simulation the Hamming distance between a fracture state at time t_n and the *initial* crack state t_0 is a monotonically increasing function of time. For the fracture state space F^h , one possible distance function is the sum of the absolute difference between the crack face opening displacements at two states, x and y

$$d_{\text{cfod}}(x, y) = \sum_{i=1}^N |\text{cfod}(x_i) - \text{cfod}(y_i)| \quad (23)$$

Unlike the metric space (E^h, d_H) , the distance function d_{cfod} in the metric space (F^h, d_{cfod}) is not necessarily a monotonically increasing function in time due to crack closure.

One application of a distance function between crack states is the quantification of the sensitivity of a pervasive failure process to initial conditions and system parameters. For an example

similar to the one presented in Section 6, consider the impact of a concrete beam by a rigid projectile with a striking velocity of 20.0 m/s. The length of the beam is 4.0 m and the thickness is 0.3 m. The RCP Voronoi mesh has a characteristic length of 12 mm with a total of approximately 6000 elements and 16000 internal edges. The results of the simulation are shown at the top of Figure 21 at a simulation time of 3.0 ms. The remaining six cases are simulations using the same mesh and material parameters but with increasingly accurate values of the striking velocity from 20.1 m/s (a difference of 0.5 percent from the reference value) down to 20.000001 m/s (a difference of 5×10^{-6} percent from the reference value). Only in the last two cases are the outer structural cracks visually identical. The distance function d_H can be used to quantify the differences in the crack states. Figure 22 gives the distance between each crack state and the reference as a function of the explicit dynamic simulation step. The last time step shown (6400) corresponds to the simulation time of 3.0 ms used in Figure 21. In all cases the distance diverges exponentially (as described by Eq. (17)) and then saturates. An accuracy of 5×10^{-9} percent in the initial striking velocity is needed to achieve an identical final crack state.

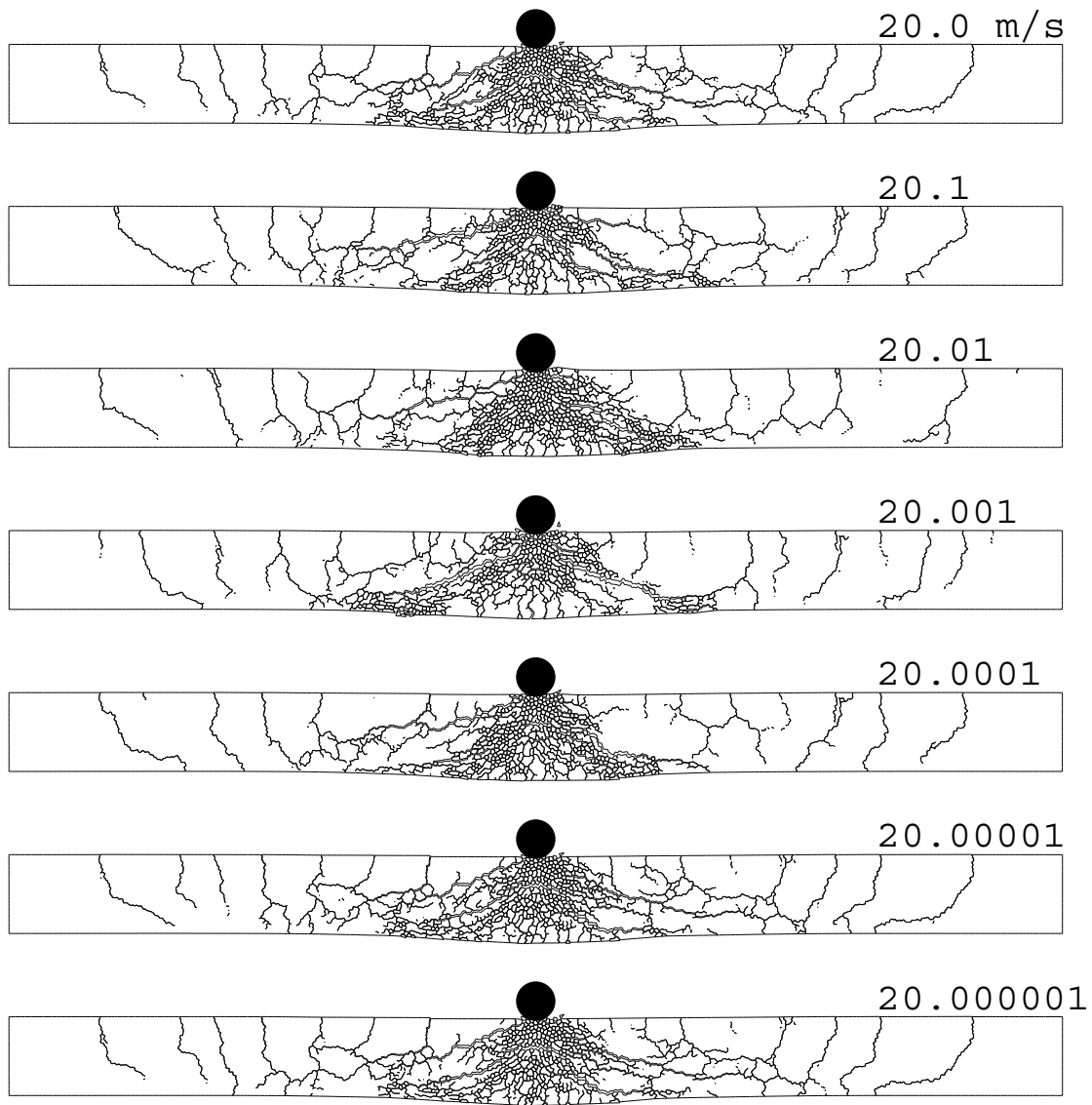


Figure 21. Crack states resulting from a rigid projectile impacting a concrete column. Each image represents the results from a different simulation using the same RCP Voronoi mesh but with a slightly different striking velocity. The time is 3.0 ms after impact which corresponds to the final simulation step (6400) reported in Figure 22.

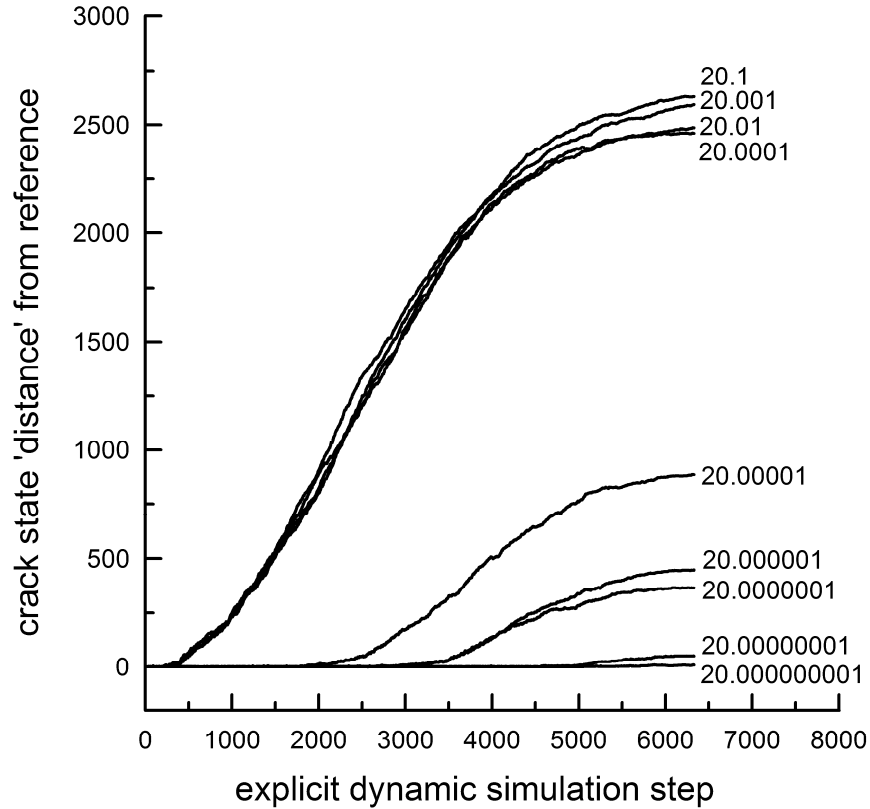


Figure 22. Distance between crack states resulting from a rigid projectile impacting a concrete column (see Figure 21) as a function of simulation step. Each curve represents a different simulation using the same RCP Voronoi mesh but with a slightly different striking velocity. Distances are with respect to the reference simulation shown at the top of Figure 21 (striking velocity = 20.0 m/s). The final simulation step (6400) corresponds to the time of 3.0 ms used in Figure 21.

7.2 graph theory and percolation

The discrete representation of fracture surfaces is ideally suited for study by graph and network theory [58]. A graph G is a pair of sets $G = \{V, E\}$, where V is a set of N vertices or nodes V_1, V_2, \dots, V_N , and E is a set of edges or links that connect the vertices of V . (The nodes and edges of the graph should not be confused with the nodes and edges of the finite element mesh.) One possible graph representation of a fracture state X is to let the nodes of the graph represent the Voronoi cells and let the edges of the graph represent whether or not a crack exists between two adjacent Voronoi cells. In this case, the nodes and edges of the graph are simply nodes and edges of the dual Delaunay triangulation described in Section 2. Another possible graph representation is to let the nodes of the graph represent a crack face pair (reference state) and let the edges of the graph represent an adjacency with another crack face pair. Once a graph structure of the fracture network is defined, the topology and statistical mechanics of the structure and its evolution could be studied using tools of graph theory including clustering, graph spectra, trees, and cycles [58].

Finally, the connectedness of a domain and its bifurcation through fragmentation is of central importance in percolation theory. Percolation theory has been a valuable tool for understanding certain critical phenomena such as phase changes and localization [59, 60]. A few studies of the application of percolation theory to fragmentation have been performed by Englman [61] using square lattices, Sokolov [62] using a regular triangular array of springs, and Astrom [63] using an irregular beam lattice. Dienes [64] studied the cluster statistics and percolation threshold of a network of cracks using a geometry based statistical crack mechanics. The application of percolation theory to characterize pervasive failure simulated using a continuum mechanics based discrete crack representation could be a fruitful avenue for further research.

8. VALIDATION APPROACH

The proposed computational approach for modeling pervasive fracture based on only allowing fractures to nucleate at interelement faces is considered to be most applicable to the modeling of fracture processes in quasi-brittle materials such as concrete in which the crack paths are tortuous, jagged, and not well idealized as smooth. An idealization of these crack as smooth is a stark contrast to a more realistic fractal representation [52, 53]. The RCP Voronoi approach has the potential to ‘converge’ to such a fractal representation. Also, as discussed in Section 6, quasi-brittle materials have a relatively large cohesive zone size. For these reasons, along with the importance of modeling failure processes in concrete structures, concrete was chosen to be the material of interest for an initial validation step. Also, quasi-static single crack growth will be studied for the initial validation step. This much simplified regime of fracture allows for a more in depth study of the statistical notions of convergence proposed in Section 5.

A common concrete fracture experiment is the displacement controlled three-point-bend test shown schematically in Figure 23 [69,71,72]. Numerous variants of this test exist including specimens with preexisting notches and variations on the constraints and loading. For the initial validation step, the quasi-static displacement controlled three-point-bend test containing a preexisting edge notch at the midsection will be used [71]. Several nominal simulations of this test were performed as shown in Figure 24. These initial simulations demonstrated the inherent difficulty in simulating a quasi-static process using explicit dynamics. For typical specimen sizes on the order of one meter and mesh sizes on the order of centimeters, the critical time step is on the order of microseconds. In order to maintain a quasi-static loading rate, physical time is on the order of seconds resulting in millions of time steps. A number of numerical techniques were incorporated in an attempt to increase the critical time step. Graded meshes were used as shown in Figure 24(a) along with nodal mass scaling. The presence of high-frequency oscillations in an explicit-dynamic simulation makes convergence calculations difficult in all but a ‘view-graph norm.’ Artificial damping was used to help control high-frequency vibrations, but this was found to be only marginally effective.

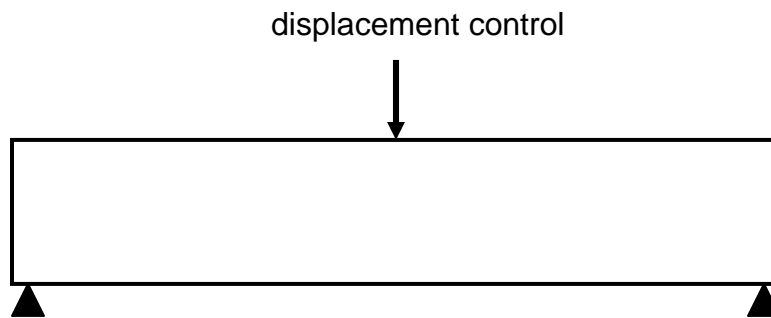
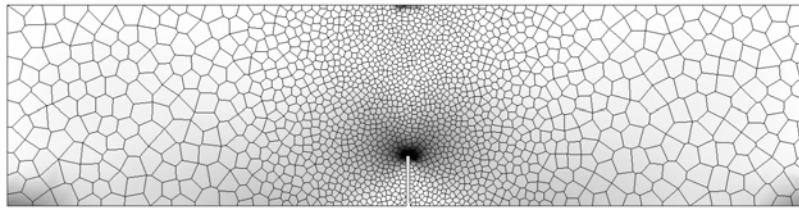


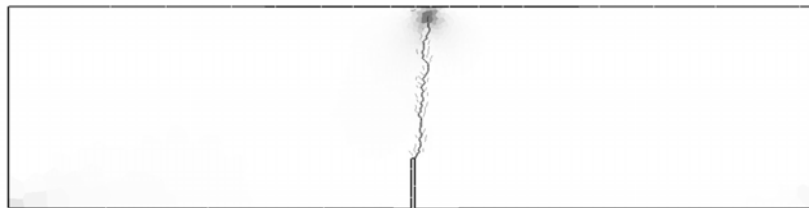
Figure 23. Schematic of a displacement controlled three-point bend test.



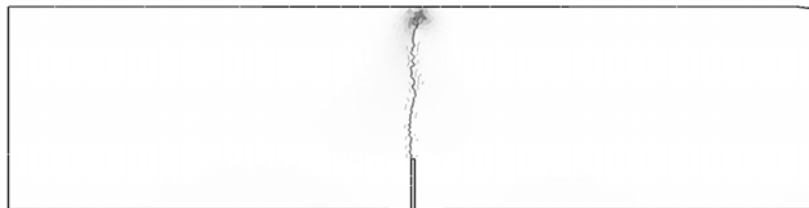
(a)



(b)



(c)



(d)

Figure 24. Simulation of a displacement controlled three-point bend experiment (a) RCP Voronoi mesh graded near the center with contoured max-principal stress field (b-d) Three separate simulations of crack growth using three different RCP Voronoi meshes with identical loading conditions.

A number of cases and comparisons are of interest. The following list of cases is given in order of increasing generality:

1. Straight crack idealization, symmetric mesh about midplane, preexisting cohesive interface elements.
2. Straight crack idealization, symmetric mesh about midplane, dynamic mesh connectivity, new cracks are restricted to the straight crack trajectory.

3. Nonsymmetric mesh, dynamic mesh connectivity, contiguous cracking only.
4. Nonsymmetric mesh, dynamic mesh connectivity, arbitrary cracking.

In case 3 ‘contiguous cracking’ constrains the interelement faces at which new cracks can form to be only those faces that are attached to an existing crack. In case 4 ‘arbitrary cracking’ connotes unconstrained fracture in that a crack can form at any interelement face. For each of these cases, the load versus displacement relationships can be compared and assessed for convergence with mesh refinement. As discussed in Section 5, it is envisioned that only the *distribution* of crack paths and load-displacement responses will be shown to be convergent. Furthermore, only the distribution of crack paths itself can be viewed as mesh independent.

Results from case 2 exhibited an immediate difficulty. The dynamic change in connectivity of the structure resulted in a relatively large artificial vibration in the structure. In a load vs. displacement plot, the vibration was roughly the same magnitude as the peak load, thus polluting the results. In high-energy impacts, this artificially induced noise is relatively small. However, in a quasi-static analysis using a dynamic solver, the artificially induced vibration is intolerable. For specific boundary-value problems, localization parameters can be adjusted to ameliorate this behavior, but there doesn’t seem to be a robust method for general dynamic problems under all regimes of stress states (compression and tension). The problem is fundamentally due to the discontinuity of tractions at the element faces and the inability to recover interelement tractions that are dynamically consistent with the nodal forces. Methods exist for recovering interface tractions from nodal forces [74] but these do not completely fix the problem. An alternative approach is presented in the next section.

9. DISCONTINUOUS-GALERKIN FORMULATION

In the computational approach based on a dynamic change in mesh connectivity, the displacement field was continuous until localization and material failure was detected at an element face whereupon the mesh connectivity was modified to represent the new localization surface. While this approach is computationally efficient, there is not a unique relationship between interface tractions, nodal forces, and element stresses. Inevitably, when the mesh connectivity is modified, there is an inconsistency between the previous nodal force state and the new nodal force state from the next time step. This results in a nonsmooth system response that can be severe in quasi-static problems as discussed in the previous section. (Note that this effect is present any method that modifies mesh connectivity in a time dependent problem. Not just fracture problems.)

One promising alternative is a *discontinuous* Galerkin (DG) approach in which the interface tractions are an integral part of the variational formulation. DG methods have found wide applicability in a variety of problems including fluid dynamics and incompressible elasticity [73]. Herein, a type of DG approach is proposed and is currently under study. The method is iterative in nature and is based on a variant of Nitsche's method used for solving contact problems [76]. The iterative approach is analogous to an augmented-Lagrangian approach for enforcing contact constraints [75]. The proposed method has been demonstrated to be convergent for the standard beam-bending benchmark problem used in Section 3. Work is ongoing to demonstrate the use of this method with a cohesive law and the validation approach discussed in the previous section.

For simplicity, the following discussion is restricted to small strains and displacements. First, a Lagrange multiplier based discontinuous Galerkin formulation will be discussed. Following this discussion, a discontinuous Galerkin formulation based on an iterative form of Nitsche's method will be presented.

9.1 Lagrange Multiplier based Discontinuous Galerkin

A simple discontinuous Galerkin formulation can be obtained by disconnecting all elements and enforcing compatibility with Lagrange multipliers at the element interfaces. The finite elements do not have to be compatible. The Lagrange multipliers represent the interelement tractions. To avoid the common numerical difficulties associated with Lagrange multipliers, an augmented formulation with a penalty stiffness can be used. The total potential energy Π is given by

$$\Pi = \Pi^{\text{bulk}} + \int_{\Gamma^{\text{int}}} \boldsymbol{\lambda} \bullet \mathbf{g} \, d\Gamma + f(h) \int_{\Gamma^{\text{int}}} \frac{1}{2} k_p \mathbf{g} \bullet \mathbf{g} \, d\Gamma \quad (24)$$

where Π^{bulk} represents the total potential energy of the continuum, Γ^{int} represents the interelement surfaces, $\boldsymbol{\lambda}$ is the vector Lagrange multiplier, \mathbf{g} is the interface gap vector, k_p is the penalty stiffness parameter, and $f(h)$ is a scalar function of the mesh size h . The function $f(h)$ is included because the interelement surface area increases with mesh refinement and is thus not intrinsic to the boundary value problem itself. The functional form of $f(h)$ is currently under

study but is expected to be dependent upon the number of spatial dimensions. In the simulations to follow a form of $f(h) = 1/h$ is used. Taking a first variation gives [75]

$$\delta\Pi = \delta\Pi^{\text{bulk}} + \int_{\Gamma^{\text{int}}} \boldsymbol{\lambda} \bullet \delta\mathbf{g} \, d\Gamma + f(h) \int_{\Gamma^{\text{int}}} k_p \mathbf{g} \bullet \delta\mathbf{g} \, d\Gamma \quad (25)$$

where $\boldsymbol{\lambda}$ is taken to be a constant updated during iteration such that

$$\boldsymbol{\lambda}^{i+1} = \boldsymbol{\lambda}^i + k_p \mathbf{g} \quad (26)$$

Note that both the Lagrange multiplier term and the penalty term in Eq. (24) are zero for the exact solution ($\mathbf{g} = 0$). This approach was implemented and shown to give equivalent results to a standard continuous Galerkin approach. In theory this approach could be used to incorporate a cohesive traction law directly in the formulation. However, the difficulty with this approach is that the Lagrange multipliers are typically not consistent with the element stresses and can even be oscillatory in space, thus giving nonphysical results. This approach is modified in the next section by borrowing an approach from Nitsche's method which has been used successfully in contact problems [76].

9.2 Nitsche based Discontinuous Galerkin

In Nitsche's method [76] the Lagrange multiplier in Eq. (24) is replaced by the average of the interelement traction vector \mathbf{T} obtained from the stress field of the attached elements as shown in Figure 25. Eq. (24) becomes

$$\Pi = \Pi^{\text{bulk}} + \int_{\Gamma^{\text{int}}} \frac{1}{2} (\mathbf{T}_1 + \mathbf{T}_2) \bullet \mathbf{g} \, d\Gamma + f(h) \int_{\Gamma^{\text{int}}} \frac{1}{2} k_p \mathbf{g} \bullet \mathbf{g} \, d\Gamma \quad (27)$$

In variational form

$$\delta\Pi = \delta\Pi^{\text{bulk}} + \int_{\Gamma^{\text{int}}} \frac{1}{2} (\mathbf{T}_1 + \mathbf{T}_2) \bullet \delta\mathbf{g} \, d\Gamma + f(h) \int_{\Gamma^{\text{int}}} k_p \mathbf{g} \bullet \delta\mathbf{g} \, d\Gamma \quad (28)$$

where the traction vector \mathbf{T} is taken to be a constant updated during iteration by the relation

$$\mathbf{T}^{i+1} = \boldsymbol{\sigma}^i \bullet \mathbf{n} \quad (29)$$

Note that both interface terms in Eq. (27) are zero for the exact solution ($\mathbf{g} = 0$). Also, note that the penalty term is not used to update the interface tractions in Eq. (29) as in Eq. (26). If the iterative scheme of Eqs. (28) and (29) converges, then there is a natural consistency between the interface tractions and elements stress field.

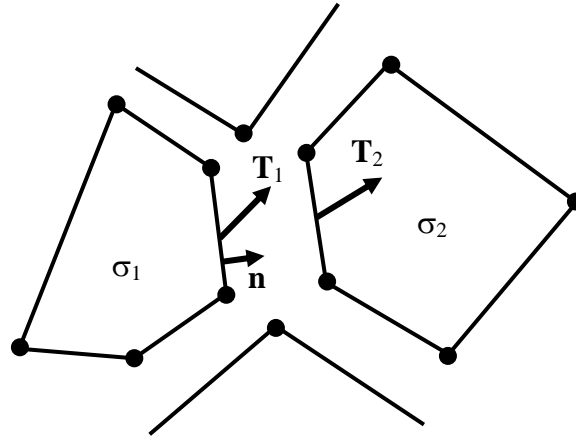


Figure 25. Schematic illustrating the interelement tractions obtained from the adjacent mean element stress.

This method was implemented for a perfect interface. An average stress state was used in each element and thus a uniform interface traction. The method was shown to pass the patch test and converge on the beam-bending verification problem of Section 3. Figure 26 gives a comparison of the L_2 norm of the displacement error for the beam-bending verification problem using both a standard continuous Galerkin formulation and a discontinuous Galerkin formulation. Ten RCP Voronoi mesh realizations were used at each refinement level. Results for the discontinuous Galerkin formulation are given for several values of the penalty parameter k_p . The convergence rate is also given and is shown to increase with increase penalty stiffness.

With these promising results, current research is focusing on incorporating a softening traction-separation law into the formulation. Once this task is complete, work will focus on completing the validation tasks outlined in Section 8.

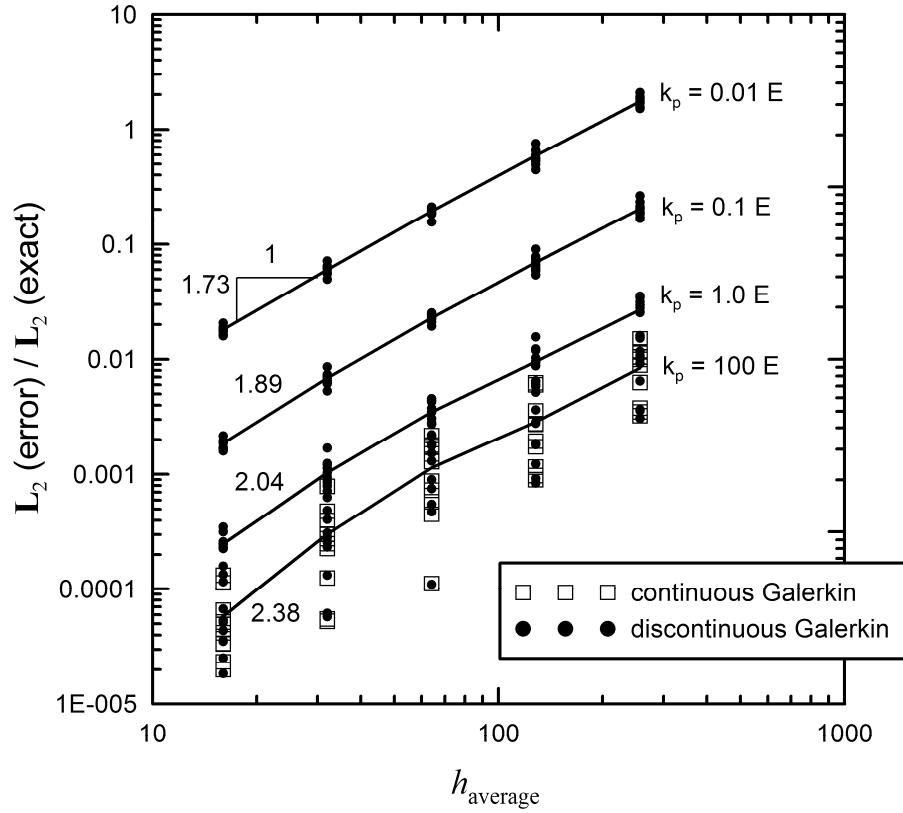


Figure 26. Comparison of the L_2 norm of the displacement error for the beam-bending verification problem using both a standard continuous Galerkin formulation and a discontinuous Galerkin formulation. Ten RCP Voronoi mesh realizations were used at each refinement level where h_{average} represents the average cell size of the RCP Voronoi mesh. Results for the discontinuous Galerkin formulation are given for several values of the penalty parameter k_p . The convergence rate is also given. (plane stress conditions, Poisson's ratio = 0.3, beam aspect ratio = 4.0).

10. SUMMARY

A pure Lagrangian computational method based on randomly close-packed Voronoi tessellations is proposed as a rational approach for simulating the pervasive fracture and fragmentation of materials and structures. Each Voronoi cell is formulated as a finite element using the reproducing kernel method. Fracture surfaces are allowed to nucleate only at the intercell faces. The randomly seeded Voronoi cells provide an unbiased network for representing cracks. In this initial study two approaches for allowing the new surfaces to initiate were studied: (1) dynamic mesh connectivity and the instantaneous insertion of a cohesive traction when localization is detected, and (2) a discontinuous Galerkin approach in which the interelement tractions are an integral part of the variational formulation but only become active once localization is detected.

A number of validation ‘first steps’ were discussed including the simulation of quasi-static three-point bend fracture experiments of concrete. It was found that in this case, the dynamic insertion process can induce relatively large nonphysical vibrations in the structure. Based on this result, a new discontinuous Galerkin approach was proposed based on an iterative form of Nitsche’s method used in contact problems.

A number of challenges exist with the approach of only allowing cracks to nucleate and propagate at interelement surfaces: (1) artificial shear-induced dilation, (2) consistency between the localization criteria, bulk constitutive models, and softening relationships, and (3) statistical measures of convergence. The mesh based shear-induced dilation could be ameliorated by the use of vertex-smoothing in the sliding-contact algorithm.

Beyond the application to weapons effects on structures, another important application of the proposed method is geomechanics. The RCP mesh with interelement fractures provides a natural basis for an ‘explicit fracture network’ that can be used for porous flow modeling. Ultimately, it could be one component in a unified coupled thermal-mechanical-hydro formulation. This capability would be particularly useful for the simulation of hydraulic fracturing in geothermal reservoirs, containment issues in CO₂ sequestration, and nuclear waste isolation.

11. REFERENCES

1. Strouboulis, T., Copps, K., and Babuska, I. (2000) 'The Generalized Finite Element Method: An Example of its Implementation and Illustration of its Performance,' *International Journal for Numerical Methods in Engineering*, 47, 1401-1417.
2. Belytschko, T. and Black, T. (1999) 'Elastic Crack Growth in Finite Elements with Minimal Remeshing,' *International Journal for Numerical Methods in Engineering*, 45, 601-620.
3. Belytschko, T., Krongauz, Y., Organ, D., Flemin, M., and Krysl, P. (1996) 'Meshless Methods: An Overview and Recent Developments,' *Computer Methods in Applied Mechanics and Engineering*, 139, 3-47.
4. Attaway, S., Heinstein, M., and Swegle, J. (1994) 'Coupling of Smooth Particle Hydrodynamics with the Finite Element Method,' *Nuclear Engineering and Design*, 150, 199-205.
5. Belytschko, T., Krysl, P., and Krongauz, Y. (1997) 'A Three-Dimensional Explicit Element-Free Galerkin Method,' *International Journal for Numerical Methods in Fluids*, 24, 1253-1270.
6. Liu, W.K., Jun, S., and Zhang, Y.F. (1995) 'Reproducing Kernel Particle Methods,' *International Journal for Numerical Methods in Engineering*, 20, 1081-1106.
7. Rabczuk, T. and Belytschko, T. (2004) 'Cracking Particles: A Simplified Meshfree Method for Arbitrary Evolving Cracks,' *International Journal for Numerical Methods in Engineering*, 61, 2316-2343.
8. Sulsky, D. and Schreyer, L. (2004) 'MPM Simulation of Dynamic Material Failure with a Decohesion Constitutive Model,' *European Journal of Mechanics A/Solids*, 23, 423-445.
9. Silling, S. and Askari, E. (2005) 'A Meshfree Method Based on the Peridynamic Model of Solid Mechanics,' *Computers and Structures*, 83, 1526-1535
10. Park, Y.K. and Fahrenthold, E. (2005) 'A Kernel Free Particle-Finite Element Method for Hypervelocity Impact Simulation,' *International Journal for Numerical Methods in Engineering*, 63, 737-759.
11. Johnson, G., Beissel, S. and Stryk, R. (2002) 'An Improved Generalized Particle Algorithm that Includes Boundaries and Interfaces,' *International Journal for Numerical Methods in Engineering*, 53, 875-904.
12. Pandolfi, A. and Ortiz, M. (2002) 'An Efficient Adaptive Procedure for Three-Dimensional Fragmentation Simulations,' *Engineering with Computers*, 18, 148-159.
13. Pandolfi, A., Krysl, P., and Ortiz, M. (1999) 'Finite Element Simulation of Ring Expansion and Fragmentation: the Capturing of Length and Time Scales through Cohesive Models of Fracture,' *International Journal of Fracture*, 95, 279-297.
14. Ruiz, G., Ortiz, M., and Pandolfi, A. (2000) 'Three-Dimensional Finite-Element Simulation of the Dynamic Brazilian Test on Concrete Cylinders,' *International Journal for Numerical Methods in Engineering*, 48, 963-994.
15. Camacho, G. and Ortiz, M. (1996) 'Computational Modeling of Impact Damage in Brittle Materials,' *International Journal of Solids and Structures*, 33, 2899-2938.
16. Ruiz, G., Pandolfi, A., and Ortiz, M. (2001) 'Three-Dimensional Cohesive Modeling of Dynamic Mixed-Mode Fracture,' *International Journal for Numerical Methods in Engineering*, 52, 97-120

17. Ortiz, M. and Pandolfi, A. (1999) 'Finite-Deformation Irreversible Cohesive Elements for Three-Dimensional Crack-Propagation Analysis,' *International Journal for Numerical Methods in Engineering*, 44, 1267-1282.
18. Zallen, R. (2004) *The Physics of Amorphous Solids*, Wiley-VCH, Ch. 2.
19. Okabe, A., Boots, B., Sugihara, K., and Chiu, S.N. (2000) *Spatial Tessellations: Concepts and Applications of Voronoi Diagrams*, John Wiley & Sons.
20. Aste, R. and Weaire, D. (2000) *The Pursuit of Perfect Packing*, Institute of Physics Publishing.
21. Finney, J. (1970) 'Random Packings and the Structure of Simple Liquids. I. The Geometry of Random Close Packing,' *Proceedings of the Royal Society of London. Series A, Mathematical and Physical Sciences*, 319, 479-493.
22. Bolander, J.E., Saito, S. (1998) 'Fracture Analyses using Spring Networks with Random Geometry,' *Engineering Fracture Mechanics*, 61, 569-591
23. Bolander, J.E. and Sukumar, N. (2005) 'Irregular Lattice Model for Quasistatic Crack Propagation,' *Physical Review B*, 71, 094106-1:12.
24. Yip, M., Mohle, J, and Bolander, J.E. (2005) 'Automated Modeling of Three-Dimensional Structural Components Using Irregular Lattices,' *Computer-Aided Civil and Infrastructure Engineering*, 20, 393-407.
25. Yip, M., Li, Z., Liao, B.S., and Bolander, J.E., (2006) 'Irregular Lattice Models of Fracture of Multiphase Particulate Materials,' *International Journal of Fracture*, 140, 113-124.
26. Bowyer, A. (1981) 'Computing Dirichlet Tessellations,' *The Computer Journal*, 2, 162-166.
27. Watson, D. (1981) 'Computing the n-Dimensional Tessellation with Application to Voronoi Polytopes,' *The Computer Journal*, 2, 167-172.
28. Rashid, M. and Selimotic, M. (2006) 'A Three-Dimensional Finite Element Method with Arbitrary Polyhedral Elements,' *International Journal for Numerical Methods in Engineering*, 67, 226-252.
29. Idelsohn, S., Onate, E., Calvo, N., and Pin, F. (2003) 'The Meshless Finite Element Method,' *International Journal for Numerical Methods in Engineering*, 58, 893-912.
30. Wachspress, E. (1975) *A Rational Finite Element Basis*, Academic Press.
31. Ghosh, S. and Mallett, R. (1994) 'Voronoi Cell Finite Elements,' *Computers and Structures*, 50, 33-46.
32. Moorthy, S. and Ghosh, S. (1996) 'A Model for Analysis of Arbitrary Composite and Porous Microstructures with Voronoi Cell Finite Elements,' *International Journal for Numerical Methods in Engineering*, 39, 2363-2398.
33. Hu, C., Bai, J., and Ghosh, S. (2007) 'Micromechanical and Macroscopic Models of Ductile Fracture in Particle Reinforced Metallic Structures,' *Modelling and Simulation in Materials Science and Engineering*, 15, 1-16.
34. Kythe, P. (1995) *An Introduction to Boundary Element Methods*, CRC Press.
35. Belytschko, T., Liu, W.K., and Moran, B. (2000) *Nonlinear Finite Elements for Continua and Structures*, John Wiley and Sons, Ch. 4.7.
36. Chen, J.S., Wu, C.T., Yoon, S., and You, Y. (2001) 'A Stabalized Conforming Nodal Integration for Galerkin Mesh-Free Methods,' *International Journal for Numerical Methods in Engineering*, 50, 435-466.
37. Hughes, T.J.R. (1987) *The Finite Element Method: Linear Static and Dynamic Finite Element Analysis*, Prentice-Hall. Ch. 4.4.

38. Hughes, T.J.R. (1987) *The Finite Element Method: Linear Static and Dynamic Finite Element Analysis*, Prentice-Hall. Ch. 4.5.
39. Belytschko, T., Liu, W.K., and Moran, B. (2000) *Nonlinear Finite Elements for Continua and Structures*, John Wiley and Sons, Ch. 6.2.
40. Hinton, E., Rock, T., and Zienkiewicz, O.C. (1976) 'A Note on Mass Lumping and Related Processes in the Finite Element Method,' *Earthquake Engineering and Structural Dynamics*, 4, 245-249.
41. Hughes, T.J.R. (1987) *The Finite Element Method: Linear Static and Dynamic Finite Element Analysis*, Prentice-Hall. Ch. 7.3.2.
42. Gallian, J. (1994) *Contemporary Abstract Algebra* 3rd edition, D.C Heath and Company.
43. Mohammadi, S. (2003) *Discontinuum Mechanics: Using Discrete and Finite Elements*, WIT Press.
44. Heinstein, M., Mello, F., Attaway, S., and Laurson, T. (2000) 'Contact-Impact Modeling in Explicit Transient Dynamics,' *Computer Methods in Applied Mechanics and Engineering*, 187, 621-640.
45. Strogatz, S. (1994) *Nonlinear Dynamics and Chaos with Applications to Physics, Biology, Chemistry, and Engineering*, Westview Press, Ch. 9.
46. Lindgren, B. (1976) *Statistical Theory*, 3rd edition, Macmillan Publishing Co., Ch. 2.5.
47. Josuttis, N. (1999) *The C++ Standard Library: A Tutorial and Reference*, Addison-Wesley.
48. Edwards, H. (2007) 'An HPC Component for Parallel, Heterogeneous, and Dynamic Unstructures Meshes,' *HPC-GECO/CompFrame 2007*, Montreal, Canada.
49. Bazant, Z.P. and Planas, J. (1997) 'Fracture and Size Effect in Concrete and other Quasibrittle Materials,' CRC Press.
50. Planas, J., Elices, M., Guinea, G., Gomez, F., Cendon, D. and Arbilla, I. (2003) 'Generalizations and Specializations of Cohesive Crack Models,' *Engineering Fracture Mechanics*, 70, 1759-1776.
51. Carpinteri, A. and Pugno, N. (2005) 'Fractal Fragmentation Theory for Size Effects of Quasi-Brittle Materials in Compression,' *Magazine of Concrete Research*, 57, 309-313.
52. Carpinteri, A., Chiaia, B. and Invernizzi, S. (1999) 'Three-Dimensional Fractal Analysis of Concrete Fracture at the Meso-level,' *Theoretical and Applied Fracture Mechanics*, 31, 163-172.
53. Perfect, E. (1997) 'Fractal Models for the Fragmentation of Rocks and Soils: a Review,' *Engineering Geology*, 48, 185-198.
54. Hornbogen, E. (1989) 'Fractals in Microstructure of Metals,' *International Materials Reviews*, 34, 277-296.
55. Bazant, Z. (2005) *Scaling of Structural Strength*, Elsevier.
56. Kreyszig, E. (1989) *Introductory Functional Analysis with Applications*, Wiley, Ch. 1.
57. Hamming, R. (1950) 'Error Detecting and Error Correcting Codes', *Bell System Technical Journal* 26, 147-160.
58. Albert, R. and Barabasi, A.L. (2002) 'Statistical Mechanics of Complex Networks,' *Reviews of Modern Physics*, 74, 47-97.
59. Creswick, R., Farach, H., and Poole, C. (1992) *Introduction to Renormalization Group Methods in Physics*, John Wiley & Sons, Inc.
60. Zallen, R. (2004) *The Physics of Amorphous Solids*, Wiley-VCH, Ch. 4.
61. Englman, R., Jaeger, Z., and Levi, A. (1984) 'Percolation Theoretical Treatment of Two-Dimensional Fragmentation in Solids,' *Philosophical Magazine B*, 50, 307-315.

62. Sokolov, I.M. and Blumen, A. 1999, 'Scaling and Patterns in Surface Fragmentation Processes,' *Physica A*, 266, 299-306.
63. Astrom, J. Holian, B., and Timonen, J. (2000) 'Universality in Fragmentation,' *Physical Review Letters*, 84, 3061-3064.
64. Dienes, J. (2006) 'On the Mean Cluster Size of a Network of Cracks,' *Structural Control and Health Monitoring*, 13, 169-189.
65. Schuster, H. and Just, W. (2005) *Deterministic Chaos, An Introduction*, 4th edition, Wiley-VCH.
66. Wiercigroch, M. and Kraker, B. (editors) (2000) *Applied Nonlinear Dynamics and Chaos of Mechanical Systems with Discontinuities*, World Scientific Publishing Company.
67. Tuffillaro, N., Abbott, T., and Reilly, J., (1992) *An Experimental Approach to Nonlinear Dynamics and Chaos*, Addison-Wesley, Ch. 1.
68. Molinari, J., Gazonas, G., Raghupathy, R., Rusinek, A., and Zhou, F. (2007) 'The Cohesive Element Approach to Dynamic Fragmentation: The Question of Energy Convergence,' *International Journal for Numerical Methods in Engineering*, 69, 484-503.
69. Cusatis, G. and Cedolin, L. (2007) 'Two-Scale Study of Concrete Fracturing Behavior,' *Engineering Fracture Mechanics*, 74, 3-17.
70. Sukumar, N. and Tabarraei, A. (2004) 'Conforming Polygonal Finite Elements,' *International Journal for Numerical Methods in Engineering*, 61, 2045-2066.
71. Horvath, R. and Persson, T. (1984) 'The Influence of the Size of the Specimen on the Fracture Energy of Concrete,' Report TVBM-5005, The Division of Building Materials, Lund Institute of Technology, Lund, Sweden.
72. Elices, M. and Planas, J. (1996) 'Fracture Mechanics Parameters of Concrete: An Overview,' *Advances in Cement Based Materials*, 4, 116-127.
73. Eyck, A. and Lew, A. (2006) 'Discontinuous Galerkin Methods for Non-linear Elasticity,' *International Journal for Numerical Methods in Engineering*, 67, 1204-1243.
74. Ciancio, D., Carol, I., and Cuomo, M. (2006) 'On Inter-element Forces in the FEM-Displacement Formulation, and Implications for Stress Recovery,' *International Journal for Numerical Methods in Engineering*, 66, 502-528.
75. Simo, J. and Laursen, T. (1992) 'An Augmented Lagrangian Treatment of Contact Problems Involving Friction,' *Computers and Structures*, 42, 97-116.
76. Wriggers, P. and Zavarise, G. (2008) 'A Formulation for Frictionless Contact Problems using a Weak Form introduced by Nitsche,' *Computational Mechanics*, 41, 407-420.

DISTRIBUTION

1		Gianluca Cusatis Department of Civil and Environmental Engineering Rensselaer Polytechnic Institute Troy, NY 12180	
1		Mark Rashid Department of Civil and Environmental Engineering University of California Davis, CA 95616	
1		Rebecca Brannon Department of Mechanical Engineering University of Utah Salt Lake City, UT 84112	
1	MS9042	M. Chiesa	8776 (electronic copy)
1		J. Foulk	8776 (electronic copy)
1	MS9404	A. Mota	8776 (electronic copy)
1	MS0372	C. Stone	1525 (electronic copy)
1		J. Arguello	1525 (electronic copy)
1		G. Peace	1525 (electronic copy)
1		J. Redmond	1525 (electronic copy)
1		J. Pott	1524 (electronic copy)
1		A. Gullerud	1524 (electronic copy)
1		J. Ostien	1524 (electronic copy)
1	MS0376	J. Rath	1524 (electronic copy)
1	MS0346	J. Cox	1526 (electronic copy)
1		D. Reedy	1526 (electronic copy)
1	MS1070	C. Wong	1526 (electronic copy)
1	MS0847	S. Attaway	1534 (electronic copy)
1	MS0380	J. Jung	1542 (electronic copy)
1		M. Heinstein	1542 (electronic copy)
1		B. Spencer	1542 (electronic copy)
1		V. Porter	1542 (electronic copy)
1		S. Key	1542 (electronic copy)
1		N. Crane	1542 (electronic copy)
1		M. Bhardwaj	1542 (electronic copy)

1	MS1160	V. Luk	5431 (electronic copy)
1		D. Dederman	5431 (electronic copy)
1		J. Foster	5431 (electronic copy)
1	MS0378	E. Strack	1431 (electronic copy)
1		A. Robinson	1431 (electronic copy)
1	MS1033	C. Hickox	6331 (electronic copy)
1	MS0744	M. Hessheimer	6764 (electronic copy)
1	MS0751	T. Pfeifle	6315 (electronic copy)
1		L. Costin	6311 (electronic copy)
1	MS1320	R. Lehoucq	1414 (electronic copy)
1	MS1322	S. Silling	1435 (electronic copy)
1	MS0899	Technical Library	9536 (electronic copy)



Sandia National Laboratories